

Nonconventional deep brain stimulation waveforms affect firing in a computational model of the subthalamic neuron

Author François Kroll¹

Director Didier Gonze²

Promotor Myles Mc Laughlin³

Academic year 2017-2018

Research conducted in Myles Mc Laughlin's laboratory, Katholieke Universiteit Leuven, Belgium

¹ Université Libre de Bruxelles (ULB), Brussels, Belgium.

Master's student in Bioinformatics and Modelling

² Unité de Chronobiologie Théorique, Université Libre de Bruxelles (ULB), Brussels, Belgium

³ Neurosciences, Katholieke Universiteit Leuven (KUL), Leuven, Belgium

Nonconventional deep brain stimulation waveforms affect firing in a computational model of the subthalamic neuron

MASTER'S THESIS

Research performed in Prof Myles Mc Laughlin's laboratory, Katholieke Universiteit Leuven, Belgium

AUTHOR: François Kroll¹

¹Université Libre de Bruxelles (ULB), Brussels, Belgium.
Master's student in Bioinformatics and Modelling

DIRECTOR: Didier Gonze²

²Unité de Chronobiologie Théorique, Université Libre de Bruxelles (ULB), Brussels, Belgium

PROMOTOR: Myles Mc Laughlin³

³Neurosciences, Katholieke Universiteit Leuven (KUL), Leuven, Belgium

Academic year 2016-2017

Abstract

Deep brain stimulation is a potent and cost-effective therapeutic alternative to medication for Parkinson's disease motor symptoms. It involves the implantation of an electrode into the subthalamic nucleus. The electrode delivers high-frequency electrical stimulation which disrupts the pathological patterns of neural signalling. The standard clinical electrical pulse has two components: a first short cathodic stimulating pulse, directly followed by a longer, lower amplitude anodic recharge phase which provides balance of charge important for safety reasons. Computational modelling plays a crucial role in the development and theoretical understanding of this technology.

Here, we set out to evaluate a series of nonconventional waveforms at a wide range of pulse widths on a model of the subthalamic projection neuron adapted from Miocinovic et al., 2006ⁱ. We mainly studied the effects of these waveforms in terms of thresholds for activation, displayed as strength-duration curves, and action potential firing sites.

Several nonconventional waveforms generated interesting behaviour, such as movement of the action potential initiation site and effects on the strength-duration curves. Placing the recharge phase before the stimulating pulse also yielded promising results, potentially evoking twice as much spikes when delivered slightly suprathreshold.

This work provides a single-cell model that can readily be used to investigate virtually any combination of nonconventional stimulation parameters. Finally, it is preceding the evaluation of these waveforms in Parkinson's disease patients. By providing reasoning examples and clues about their mechanisms, we hope that it will contribute to a better understanding of the clinical effects of nonconventional waveforms and help in the formulation of hypotheses with regard to their efficacy.

ⁱ Miocinovic, S. *et al.* Computational analysis of subthalamic nucleus and lenticular fasciculus activation during therapeutic deep brain stimulation. *J. Neurophysiol.* **96**, 1569–1580 (2006).

Contents

Literature review	1
Parkinson's disease.....	1
Medication treatment	1
Deep brain stimulation	2
Stimulation parameters.....	6
Strength-duration curve	7
Waveform.....	8
Neuron modelling.....	9
The NEURON simulator	11
Aim of the study.....	12
Material and methods.....	14
STN projection neuron model	14
Morphology files	14
Mechanism files	16
The electric field files.....	16
The waveform files	17
The main file	17
Simulations	18
Waveforms.....	19
Development of the model and data processing.....	21
Explanations.....	21
Waveform files	21
Strength-duration curve	21
Initiation sites bubble graph	22
Latency times scatter plot.....	24
Graphics.....	24
Results and discussion	25

Monophasic waveforms serve as control.....	25
The recharge phase of the clinical anodic waveform is not passive at long pulse widths.....	29
At short pulse widths, the anodic postpulse waveform moves the initiation site without affecting the strength-duration curve.....	33
The prepulse anodic waveform may be useful to double the firing rate at minimum energy cost.....	36
Biphasic waveforms show superiority of cathodic stimulation.....	41
Future directions.....	44
Towards further use of the model.....	44
Further development of the model	44
Further testing of nonconventional parameters	46
Towards clinical use	47
Conclusion	48
Bibliography.....	49
Supplementary figures.....	52

Abbreviations

AP	Action potential
DBS	Deep brain stimulation
FLUT	Fluted region
GPI	Internal globus pallidus
Hoc	High Order Calculator (language)
MYSA	Myelin sheath attachment
ODE	Ordinary differential equation
PD	Parkinson's disease
SNpc	Substantia nigra pars compacta
STIN	Stereotyped internode
UPDRS	Unified Parkinson's disease rating scale
STN	Subthalamic nucleus

Literature review

Parkinson's disease

Parkinson's disease (PD) is a progressive neurodegenerative disorder. It is the most common after Alzheimer's¹. Today, more than 2 million people live with PD in Europe², and this number is expected to double by 2030³.

The main symptoms of PD are motor. They include tremor, rigidity, bradykinesia (slow movements), akinesia (inability to initiate movements), and postural instability. Tremor is undoubtedly the disease's most well-known symptom. It is also the most common: around 70% of the patients show tremor at disease onset, and most will develop it as the disease progresses. PD is also accompanied by various non-motor symptoms such as cognitive impairment, depression and sleep disorders⁴.

Although PD's pathology is now recognized as much more complex, the crucial feature remains the loss of dopaminergic neurons within the substantia nigra pars compacta (SNpc). This loss results in dopamine deficiency within the basal gangliaⁱ, which in turn leads to movement disorders¹.

At the cellular level, PD is characterized by the aggregation of a misfolded version of the protein α -synuclein, which forms intracellular inclusions called Lewy bodies. Although it certainly participates, Lewy pathology alone does not account for neuronal loss, which remains poorly understood¹.

There is currently no treatment able to stop or slow the disease progression. The only available therapies treat the symptoms of the disease¹.

Medication treatment

The mainstay for motor symptom management are drugs that increase intracerebral dopamine concentrations or stimulate dopamine receptors. One of the most widely used is levodopa. Nearly all patients with PD will use it at some point. Levodopa (or L-DOPA for L-3,4-dihydroxyphenylalanine) is an amino acid precursor of the deficient neurotransmitter dopamine. It is able to cross the blood–brain barrier, while dopamine cannot⁵.

ⁱ The basal ganglia is a group of subcortical nuclei that include, among others, the globus pallidus, the substantia nigra and the subthalamic nucleus. These nuclei are strongly interconnected with the cerebral cortex, the thalamus and the brainstem⁶¹ (Figure 2).

Rigidity and bradykinesia are usually suppressed by levodopa. Response to tremor, on the other hand, is more variable, and non-motor symptoms respond rather poorly⁵.

Benefits of levodopa on symptoms do not fade as the disease progresses. However, the drug's adverse effects spread and intensify. The main motor complications of levodopa are dyskinesia (involuntary movements) and motor fluctuations. Around 50% of the patients will experience either or both after 5 years of treatment. Motor fluctuation is the resurgence of PD motor symptoms before the expected end of levodopa activity. As PD takes its course, levodopa's effects last for shorter periods of time. The effects of levodopa also take longer to appear so the therapeutic window gets truncated at both ends⁵.

Once levodopa-induced dyskinesia has appeared, treatment often becomes unsatisfactory. One solution at this point is surgical interventions such as deep brain stimulation⁵.

Deep brain stimulation

Before the discovery of levodopa, surgical procedures were the only efficient way to treat PD motor symptoms. They consisted of lesioning the pyramidal tracts⁶. Pyramidal tracts are aggregations of efferent nerve fibres from the upper motor neurons. These neurons originate in the cerebral cortex and terminate in the spinal cord or brainstem⁷. The fibres were lesioned either at their point of origin in the cortex, or further down closer to the brainstem or the spinal cord. Tremor was reliably improved, although hemiparesis (unilateral paresis) was an unavoidable consequence⁶.

In 1952, while performing a surgical procedure on a PD patient, Dr. Irving Cooper accidentally incised the anterior choroidal artery responsible to supply several brain structures including the globus pallidus. Although the artery was quickly ligated, the patient showed a reduction in rigidity and tremor with unaffected motor and sensory function. Cooper deduced that these benefits were caused by infarction (tissue death due to interruption of blood supply) of the globus pallidus. Together with the development of complementary methods, ablative procedures grew in popularity as a result, even though they often resulted in irreversible deficits in speech, swallowing and cognition⁶.

When levodopa was discovered in the early 1970s, ablative surgical interventions faded in popularity. Thereafter, the realization that patients develop complications induced by the drug sparked a resurgence of interest for surgical procedures. In 1987, Dr. Alim-Louis Benabid received a PD patient who had already undergone contralateral ablation for tremor. He was concerned about producing bilateral lesion and thus tried another approach. He implanted an electrode into the untreated thalamus and connected it to an external battery. By injecting high-frequency electrical stimulation through the electrode, his team was able to suppress tremor as effectively as ablative surgery⁶.

Deep brain stimulation (DBS) is now used as a potent therapeutic alternative in advanced stages of PD when medications are no longer satisfactory. It involves a surgical procedure in which an electrode is implanted into a specific region of the brain. The electrode consists in the tip of a wire and commonly has four active contacts. The wire exits through a burr hole drilled into the skull and passes under the skin of the scalp and the neck to join the pulse generator implanted in the chest below the clavicle (**Figure 1**). The pulse generator delivers high-frequency electrical stimulation which is believed to disrupt the abnormal patterns of neural signalling⁶.

The targeted structure can either be the subthalamic nucleus (STN) (**Figure 1**) or the globus pallidus (GPi) (**Figure 2**). Despite some significant differences, they both provide fairly equivalent benefits⁸. The decision is mainly patient-specific and should be the result of a comprehensive evaluation⁶. This work will solely focus on the STN: it is by far the most common target⁹, including in the university hospital where this study was conducted (UZ Leuven).

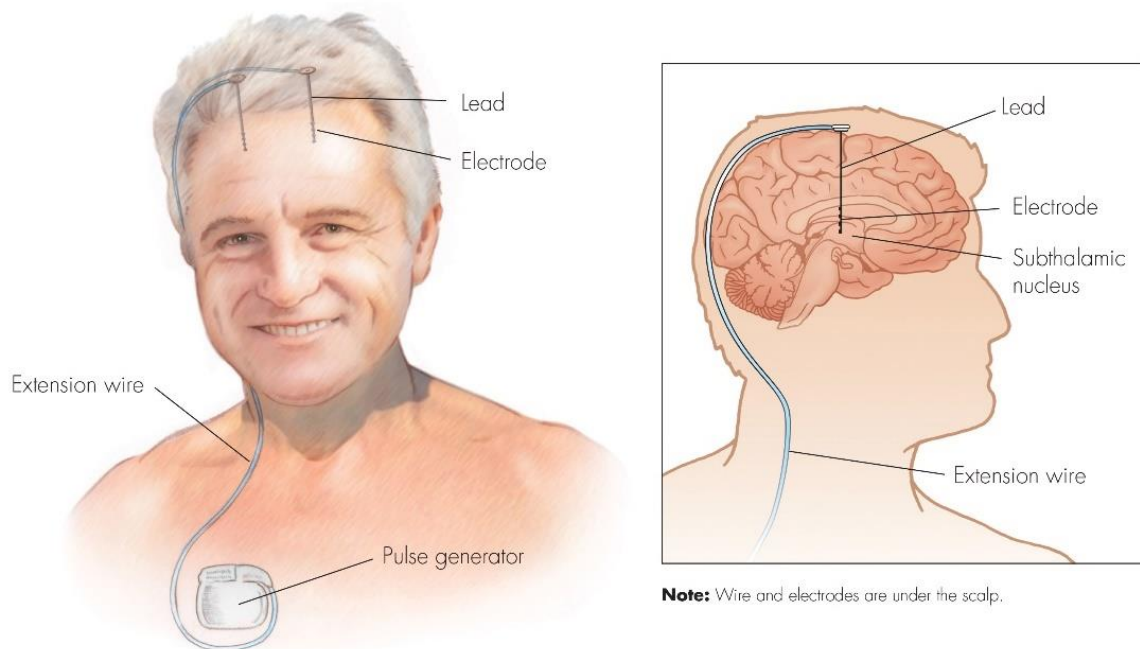


Figure 1 | Illustration of bilateral STN DBS. The electrodes are implanted in the subthalamic nucleus, and connected via a wire to the pulse generator located in the patient's chest (adapted from UC Regents, 2015⁶²).

The results are usually striking with a reduction in both the PD motor symptoms and the adverse effects induced by levodopa^{6 10}. DBS reliably improves tremor, rigidity, bradykinesia and levodopa-induced dyskinesia and motor fluctuations. Postural instability has a more variable response¹⁰.

The efficacy of deep brain stimulation on PD motor symptoms has been assessed in multiple randomized controlled trials. Quality of life and motor score, as assessed by the unified Parkinson's disease rating scale (UPDRS)¹¹, both reliably increase thanks to DBS. Another important benefit of DBS used in combination with levodopa is the improvement in more than half of the patients of motor function during the "off" state, i.e. when levodopa is not effective. Patients would otherwise experience at these moments the most distressing motor symptoms but may be able to stay active thanks to DBS^{6 12}.

At present, DBS is usually considered only for patients with advanced PD who developed complications to medication. Indeed, patients who undergo surgery have a mean disease duration of 12 years. However, DBS is notably more cost-effective than medication alone in the long term and earlier implementation may prevent the development of motor complications or even slow the progression of the disease. Accordingly, several studies urge to consider DBS earlier in the disease course or even right after diagnosis^{6 13 14}.

The mechanism underlying the efficacy of DBS is debated. To coordinate with the comparable results obtained by surgical lesions, the earliest hypotheses proposed that high-frequency stimulation switches off the STN, causing a kind of functional lesion and thus decreasing output from the region. STN inhibition was indeed detected in both animal models and humans. The picture rapidly gained in complexity though. Different techniques recorded a clear activation of the GPi, which receives excitatory afferents from the STN (**Figure 2**). Simultaneous inhibition of the stimulated structure and activation of the downstream nuclei represented an apparent paradox, to which modelling studies provided a solution. When the STN neuron is placed in the electric field, stimulation-induced action potentials (APs) do not initiate in the soma as expected but further down the axon. This observation can explain how the cell body can be inactive while at the same time delivering output to the downstream nuclei. Initiation of APs in the axon also synchronizes to the electrical pulses. Overall, DBS would operate by overriding the target structure's irregular, pathological activity; replacing it by a stimulation-induced regular pattern that helps the processing of sensorimotor information and neutralizes PD symptoms¹⁰.

This theory is above all a framework. DBS produces a complex web of excitatory and inhibitory effects that modulate the entire surrounding network (**Figure 2**). The full answer is thus unlikely to be straightforward¹⁰.

DBS can be helpful in a myriad of other conditions than PD: it is commonly used for essential tremor and dystonia, and could potentially be helpful for dementia, epilepsy, stroke recovery, headache, obesity, addiction, obsessive-compulsive disorder, Tourette syndrome and depression¹⁰.

In summary, DBS is a validated, cost-effective therapy against PD motor symptoms. Nevertheless, it is not flawless.

DBS has several limitations. First, it will globally act on the same symptoms than levodopa. Stated differently, symptoms which were resistant to levodopa are unlikely to be any more responsive to DBS⁶. As explained, implantation is also an invasive procedure. As any surgery, it involves limited risks of haemorrhage and infection¹⁰. Moreover, the pulse generator's battery must be replaced every three to five years, which involves each time another minor surgery¹⁵. DBS also involves frequent follow-up visits and programming sessions, especially if adverse effects appear. Even though generally transient and reversible, they are another important limitation to DBS. They may include swallowing¹⁶ and speech deficits, spontaneous contractile movements and mood disturbances such as mania, depression¹⁷ and apathy. Most of them are

caused by undesired stimulation of structures neighbouring the target⁶. The STN being a small nucleus surrounded by several major tracts of fibres (**Figure 2**), specificity is indeed difficult to achieve. Activation of the corticospinal tract within the internal capsule, for instance, causes the undesired muscle contractions. Paradoxically, the spread of stimulating current into adjacent regions also has beneficial effects and is thought to be a component of DBS mechanism on PD symptoms¹⁸.

Positioning errors of 2 mm or less may be sufficient to produce side effects that overshadow DBS's benefits. For this reason, the patient undergoes extensive neuroimaging prior to surgery. This allows the neurosurgeon to delimit the desired target and select an adequate entry point in the skull⁶. Successful therapy is also highly dependent on the stimulation parameter selection. Settings are explored with the patient during programming sessions. The goal is to identify those that maximize the therapeutic benefits while minimizing side effects and current consumption⁶.

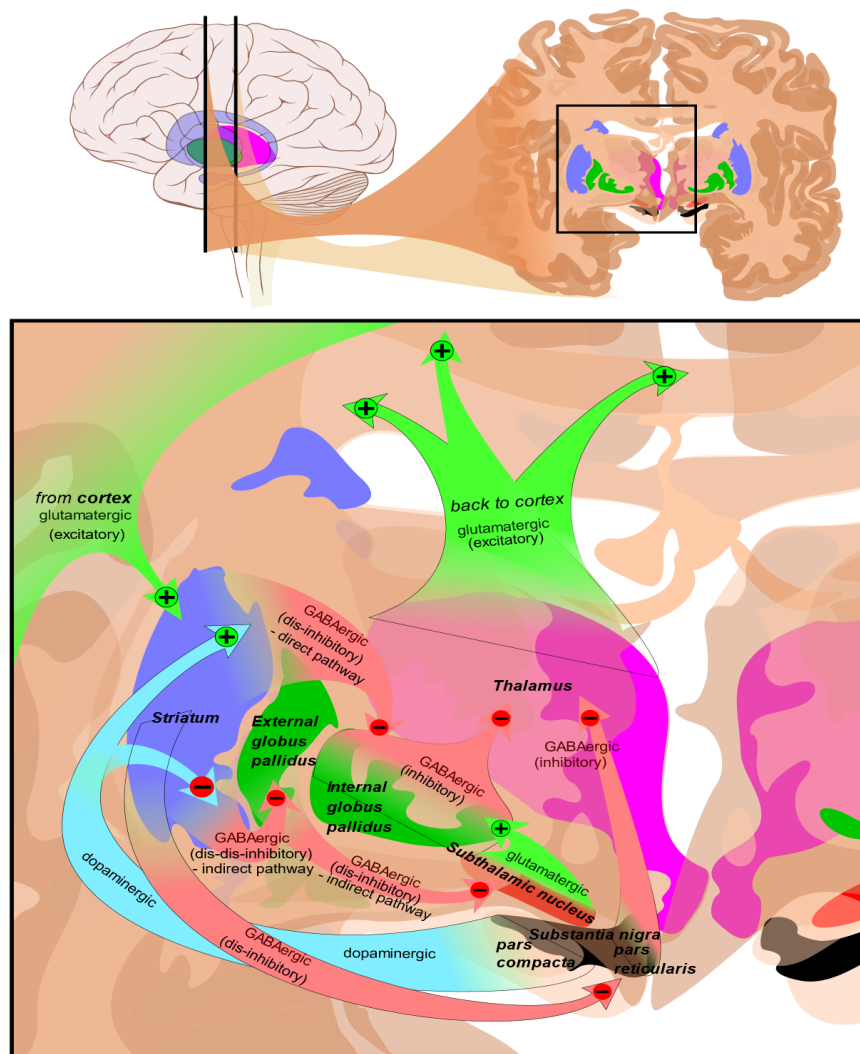


Figure 2 | Anatomy and main circuits of the basal ganglia. The mentioned nuclei include the thalamus, the substantia nigra pars compacta (SNpc), the internal globus pallidus (GPi), and the subthalamic nucleus (STN) (adapted from Häggström, 2010⁶³).

Stimulation parameters

After surgical localisation, selection of the appropriate stimulation parameters is probably the next most determining factor to successful DBS¹⁹. Four parameters can be distinguished.

Amplitude

Pulse amplitude is expressed in volts (V) and corresponds to the amplitude of stimulation.

Negative voltage implies cathodic stimulation, while positive voltage implies anodic stimulation. However, it is typically given as an absolute value.

Typical values for amplitude are 1–5 V^{20 21} (**Figure 4**).

Frequency

Frequency is expressed in Hertz (Hz) and corresponds to the number of electrical pulses per second.

Typical values for frequency are 120–180 Hz^{20 21}.

Pulse width

Pulse width is expressed in milliseconds (ms) and corresponds to the pulse duration.

Typical values for pulse width are 0.06–0.2 ms^{20 21} (**Figure 4**).

Electrode polarity

Polarity describes how current flows through the device. There are two possible stimulation polarities: monopolar and bipolar⁶.

In monopolar stimulation, an active contact on the electrode is set as the negative pole, i.e. the cathode; and the internal pulse generator is set as the positive pole, i.e. the anode. The result is a wide electric field with current spreading out in all directions around the electrode as it must find a path to the distant internal pulse generator (usually located in the abdomen or chest)⁶.

In bipolar stimulation, an active contact on the electrode is the cathode and another one is the anode. This creates a narrower electric field, as the current simply flows from one electrode in the brain to the other nearby electrode⁶.

Strength-duration curve

Among these parameters, the relationship between current amplitude and pulse width is one of the most important principle of electrophysiology. As current amplitude decreases, a longer pulse is needed to stimulate the neuron. Oppositely, as pulse duration decreases, a stronger pulse is needed to produce the same effect. When the minimum current amplitude necessary to evoke APs, i.e. the amplitude threshold, is plotted as a function of pulse width, the result is a non-linear relationship known as the strength-duration curve. For most neural elements, it has the shape of an exponential decay (**Figure 3**). Two pieces of information can be extracted from the strength-duration curves: the rheobase and the chronaxie. The rheobase is the current amplitude necessary to stimulate the neuron at very long, in theory infinite, pulse widths. The chronaxie corresponds to the pulse duration necessary to stimulate the neuron when amplitude is twice the rheobase. The chronaxie is a measure of the excitability of a neural element: the higher the chronaxie, the higher the amplitude or pulse width must be to activate the structure. It is commonly used as a tool to distinguish different types of neural tissues or elements²². For instance, myelinated axons have chronaxies around 30–200 μ s, while somas and dendrites' chronaxies are 1–10 ms. This explains why the short pulse widths used with DBS are unlikely to affect other structures than the axon, and more specifically the nodes of Ranvier²³.

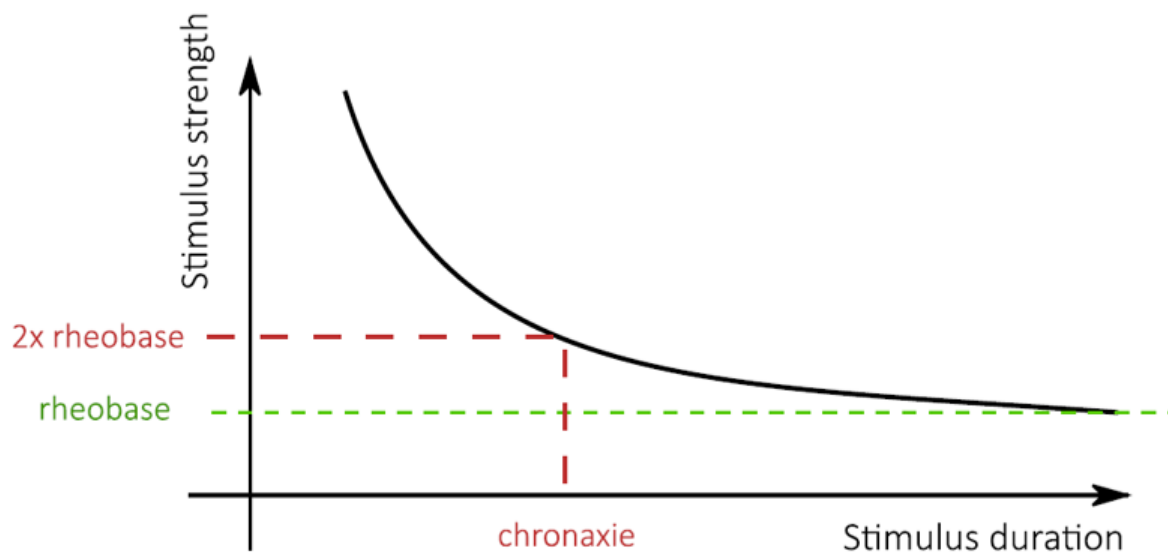


Figure 3 | Typical strength-duration curve. The rheobase (in green) is the current amplitude necessary to stimulate the neuron at very long pulse widths. The chronaxie (in red) is defined as the pulse width necessary to stimulate the neuron at twice the rheobase (adapted from Radević, 2012⁶⁴).

Waveform

Waveform describes the shape of the stimulation pulse across time. It can be described in terms of voltage and pulse width.

A fundamental rule governing waveform is the balance of charge. As current is discharged by the electrode, electrochemical reactions occur at the electrode–tissue interface. They can cause metal dissolution, which eventually corrodes the electrode and produces chemical species toxic to the surrounding cells. To prevent this from happening, the stimulating pulse is subsequently balanced by a pulse of equal but opposite charge, i.e. cathodic if the stimulating pulse is anodic, or vice versa²⁴.

The standard clinical waveform consists of a cathodic stimulating phase directly followed by a longer, weaker anodic phase providing the balance of charge²⁵. Typically, the cathodic stimulating phase is actively delivered by the internal pulse generator while the anodic phase is passive. More practically, the system stimulates across a capacitor which stores charge during stimulation. It will then release it during the anodic recharge phase to passively balance the charge injection. This ensures charge compensation and gives the anodic phase its distinct shape²⁶ (**Figure 4**).

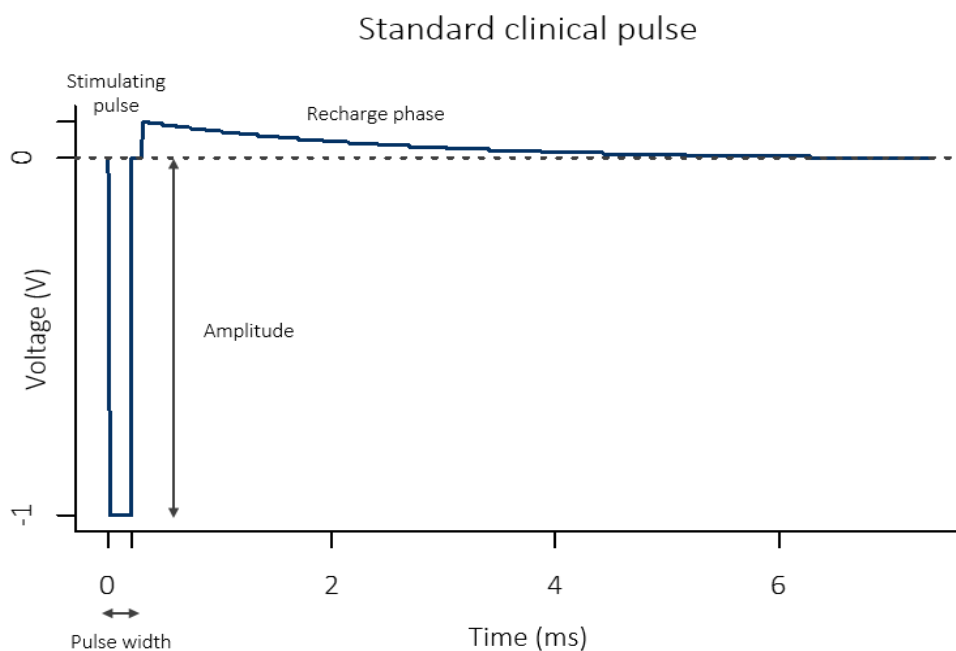


Figure 4 | The standard DBS clinical pulse. The cathodic stimulating pulse is directly balanced by the anodic recharge phase (pulse width: 0.2 ms, amplitude: 1 V).

Optimal parameters selection is typically a trial and error process performed during the programming sessions. It is, however, not feasible to scan each of the thousands possible combinations of parameters with the patient. For this reason, computer models are continuously developed to help in understanding the effects of these settings. As we have seen, computational modelling as a whole plays a crucial role in the development and theoretical understanding of DBS.

Neuron modelling

One branch of computational neuroscience relies on cable theory, a set of mathematical models describing electrical behaviour of cables²⁷. Cable theory was first developed in the 1850s to model underwater telegraphic cables²⁸.

The main result of the cable theory is a second-order partial differential equation known as the cable equation. It describes the relationship between current and voltage in a one-dimensional cable²⁷:

$$\frac{\partial V}{\partial t} + I(V, t) = \frac{\partial^2 V}{\partial x^2}$$

where V is voltage; t is time; I is current; and x is position.

Numerically solving the cable equation is the main computational task of many neuronal simulations²⁷.

For this purpose, the neuron being simulated is spatially discretised into compartments and conceptualized as an electrical circuit. Each compartment acts like a junction of the circuit.

Kirchhoff's current law, itself based on the principle of conservation of electric charge, states that at any junction in the electrical circuit, the sum of currents leaving the junction must be equal to the sum of currents entering the junction²⁷. It can be written informally for the j^{th} compartment as:

$$\sum I_{out_j} = \sum I_{in_j}$$

By replacing both sides by formulations of currents, an ordinary differential equation (ODE) is produced. It is, for the j^{th} compartment, of the form²⁷:

$$C_j \frac{dV(t)_j}{dt} + I_{ions_j} = \sum_k \frac{V_k - V_j}{R_{jk}} \quad (1)$$

The left-hand side is the total membrane current leaving the compartment. It is the sum of the capacitive and ionic components²⁷.

The capacitive component is given by the voltage/current relationship inside a capacitor:

$$I(t) = C \frac{dV(t)}{dt}$$

where C is the membrane capacitanceⁱ.

ⁱ Capacitance, expressed in farads (F), measures the ability of a body to store an electric charge. In this case, the body is the compartment's cell membrane.

The ionic component I_{ions} includes all currents flowing through ionic channel conductances^{i 27}.

Ionic currents are usually modelled by Hodgkin and Huxley's set of ODEs. For instance, the current through the voltage-gated sodium channels at a given time is described by:

$$I_{Na} = \bar{g}_{Na} m^3 h (V_m - V_{Na})$$

where I_{Na} is the sodium ionic current; \bar{g}_{Na} is the maximal conductance; m and h are dimensionless quantities between 0 and 1 representing respectively sodium channels' activation and inactivation; V_m is the membrane potential; and V_{Na} is the sodium reversal potential^{ii 29}.

m and h are described across time by:

$$\begin{aligned} \frac{dm}{dt} &= \alpha_m V_m (1 - m) - \beta_m V_m m \\ \frac{dh}{dt} &= \alpha_h V_m (1 - h) - \beta_h V_m h \end{aligned}$$

where α and β are rate constants depending on voltage, but not time²⁹.

The right-hand side of equation (1) is the total membrane current entering the compartment from adjacent ones:

$$I_{in_j} = \sum_k \frac{V_k - V_j}{R_{jk}}$$

It is an expression of Ohm's law $I = \frac{V}{R}$ at the j^{th} compartment: V_k is the voltage at the k^{th} compartment adjacent to the j^{th} compartment; V_j is the voltage at the j^{th} compartment; and R_{jk} is the resistanceⁱⁱⁱ of the resistor connecting the j^{th} and k^{th} compartments.

The neuron modelling software will approximate the longitudinal spread of voltage and current, i.e. the cable equation, by modelling the neuron as a series of compartments connected by resistors. Time is also discretised into time steps during the simulation. At each time step and each compartment, the simulator will compute equation (1) to track voltage across time and space in the neuron (e.g. **Figure 8**).

ⁱ Conductance, expressed in siemens (S), measures the ease with which an electrical current passes through an electrical conductor, in this case the cell membrane's ionic channels.

ⁱⁱ The reversal potential of an ion, also known as the Nernst potential or equilibrium potential, is the membrane potential at which there is no net flow of that ion from one side of the membrane to the other. For a typical mammalian neuron, the sodium reversal potential is around +60 mV.

ⁱⁱⁱ Resistance, expressed in ohms (Ω), measures the difficulty with which an electrical current passes through an electrical conductor, in this case the compartment's cell membrane. Resistance and conductance are the inverse quantities of each other.

The NEURON simulator

One of the most commonly used neuron modelling software around the world is NEURON³⁰

It is an open-source simulation environment, primarily designed for modelling individual neurons. It was developed by Michael Hanes and Ted Carnevale at Yale University²⁷.

NEURON has three main advantages over general purpose simulation programs. First, the user does not have to adapt the problem into another field but may keep on reasoning with concepts familiar to neuroscience. Practically, NEURON makes a clear distinction between the biological units and the mathematical compartments. The user primarily works with sections, which represent the neuron's components such as the soma or a node of Ranvier. Each section is then divided into compartments, called segments. The number of segments per section, and thus their size, is specified by the user. Sections are connected to form any kind of tree structure representing the neuron²⁷. Second, NEURON has built-in functions that are tailored specifically for controlling the simulation and plotting results in real time. Third, simulations are particularly efficient thanks to integration methods which take advantage of the structure of nerve equations²⁷.

NEURON's main scripting language is hoc, an acronym for High Order Calculator. NEURON contains numerous default mechanisms and point processes such as ionic channels, voltage clamp and AP counter. The user can also add customised point processes, such as non-default membrane channels, using the NMODL language, which will automatically be compiled into C by a built-in translator²⁷.

NEURON has numerous other interesting functionalities which ease its learning and its use, such as its graphical user interface or its shell²⁷.

Aim of the study

As mentioned previously, although DBS is a validated and widely used therapy, it has certain limitations. There are thus opportunities for further development.

The first challenge is the enhancement of efficacy. Namely, to improve the effect of DBS on motor symptoms while limiting stimulation-induced side effects. Indeed, around 30% of patients do not experience significant changes in their motor function after surgery³¹, and stimulation-related side effects are common: they include depression and mood disturbances in around 8% of patients, decrease in verbal fluency in around 30% of patients, and postural instability/gait dysfunction in up to 35% of the patients undergoing STN DBS³². These are mainly caused by spread of current causing unwanted stimulation of neighbouring structures or passing fibres from other brain regions. This is especially the case if the electrode placement is suboptimal⁶ (see *Deep brain stimulation* section). Nevertheless, these results should be interpreted with caution. DBS is generally followed by a reduction, sometimes complete, in the use of dopaminergic medication. It is thus extremely difficult to untangle what is indeed caused by DBS alone and what is a consequence of reduced levodopa use³².

The second challenge is the enhancement of DBS efficiency. The impulse generator is energy-intensive. Consequently, the battery must be replaced every three to five years depending on the stimulation parameters, although the same electrodes can be left in place and connected to a new stimulator. Over 30 years, the device would have to be replaced about 8–10 times³³. Each replacement involves an expensive and invasive surgery, which includes risks of haemorrhage and infection³³. Devices with rechargeable batteries exist, but still need replacement every 7–9 years in addition to the frequent recharges³². Alternatively, improved efficiency could also be used to reduce the volume of the device²⁶ or allow more energy to be available to implement more sophisticated functions such as closed-loop programming or directional steering of the electric field^{6 25}.

Previous studies have shown that nonconventional approaches to stimulation may have benefit. For instance, shorter pulse widths³⁴ or irregular stimulation frequencies³⁵ may both extend the battery life and improve clinical efficacy. A few studies have tested alternative waveforms on computer models, with promising results mainly concerning efficiency^{25 26 33 36}. Very few clinical trials of nonconventional settings in PD patients exist³⁷.

We set out to adapt a computational model of the STN projection neuron so it could readily be employed to evaluate alternative stimulation parameters such as nonconventional waveforms and varying pulse widths. Single neuron or even single myelinated axon models are common

practice in literature^{26 36} and are adequate to study some fundamental principles of neuronal stimulation.

We demonstrated the usefulness of this approach by testing a series of ten waveforms, many of which were not found ever tested in a similar set up in literature. We focused on testing these waveforms at a wide range of pulse widths. We first studied the influence of waveform and pulse width on threshold for activation of the neuron (see *Strength-duration curve* section). For this purpose, we generated the strength-duration curve for each waveform. It is a valuable starting point to understand how the neuron reacts to the waveform. As we will see, they allow us to estimate efficiency and they are useful to gain some insight into the mechanisms by which APs are generated.

We then sought to determine the effects of waveforms and pulse width on the APs' initiation sites. Some results exist in a thalamocortical relay neuron model, but not at this level of detail²¹. We think this approach may have merit to help in the understanding of mechanisms of DBS and suggest hypotheses, as will be explained in the *Results and discussion* section. Focus on the initiation site already bore fruit in the past when it proposed a solution to the paradox of inhibition of the targeted structure with activation of downstream nuclei¹⁰ (see *Deep brain stimulation* section).

Finally, this work will precede the testing of similar nonconventional settings on PD patients with implanted DBS devices. This trial is already planned to take place in Prof Mc Laughlin's laboratory at KU Leuven. Both approaches are complementary: the computational model provides details at the single-cell scale but does not inform on the output of the complete system; patient testing, on the other hand, reveals the effect on PD symptoms, but does not bring any information with regard to the mechanism of action. By catching a glance at both ends of the spectrum, namely at the smallest possible scale and at the largest possible scale, we may be able to infer some hypothetic mechanisms. Most articles focused on creating or testing new waveforms with the use of computational models^{25 26 33 36 38} or on testing in patients unconventional settings not previously assessed in computational models³⁷, but both approaches are rarely used in tandem. More practically, this preliminary work may also help in identifying waveforms or parameters worth further investigating in patients.

Material and methods

STN projection neuron model

The first goal of this work was to find a suitable computational model of the STN projection neuron which could be adapted for our study. For this purpose, we performed a query in the ModelDB³⁹ with keywords “*subthalamic*” and “*deep brain stimulation*”. Nine models were retrieved. Among them, six were written for other simulation environments than NEURON, which we wanted to use based on previous experience with the software. Based on the corresponding articles, we concluded that one of these three models was particularly well suited to our goals (Miocinovic et al., 2006, accession number: 151460), and proceeded to download it.

This model was originally created to study the activation of neighbouring nuclei and fibre tracts around the STN. It is mainly based on the study of DBS in parkinsonian macaques. The original article describes three fundamental components to this model: a 3D anatomical model of the monkey basal ganglia; a finite element model of the DBS electrode and the electric field it produces; and a multicompartment biophysical model of three reconstructed STN projection neurons with GPi and internal capsule fibres of passage⁴⁰. Unfortunately, many of these files are not shared on the ModelDB. Only the three multicompartment STN neuron models and the files describing the electric field are available, with little information. A preliminary task was thus to thoroughly understand the workings of the model and how the different files interact. This is explained hereafter by reviewing the important components of the model.

Morphology files

There are three morphology files in hoc language: type 1, type 3 and type 4. Each set up a different 3D geometry of the STN projection neuron. The morphology file is read by NEURON and is used to create and connect the neuron’s sections. Each section is defined by a minimum of two circles, each encoded by four values: X Y Z coordinates and a diameter value. The type 1 morphology file contains 508 sections: 3 soma sections, 288 dendrites, 28 nodes of Ranvier, 54 MYSA (myelin sheath attachment), 54 FLUT (fluted region), and 81 STIN (stereotyped internode). The STIN corresponds to the internode where the axon is tightly ensheathed by myelin. The FLUT is the juxtaparanodal region, i.e. the region adjacent to the paranode region. The MYSA corresponds to the paranodal regions, where the myelin sheath terminates in paranodal loops. Finally, the node of Ranvier is a 1- μ m section stripped of myelin between successive paranodes⁴¹ (**Figure 5**). Each section contains one mathematical segment (see *The NEURON simulator* section).

The morphology file is also used to set up the intracellular and extracellular ions concentrations, position the ions channels and specify their conductances. Intracellular ions concentrations are typical values for mammalian neurons⁴², while extracellular concentrations originate from an *in vitro* recording study of the rat subthalamic neuron⁴³. Conductances were derived from a computational study of the rat subthalamic projection neuron⁴⁴ and allow the modelling of the spontaneous activity, i.e. in the absence of excitatory input, observed during *in vitro* recordings. Indeed, the neuron model fires spontaneously at approximately 32 Hz, which is consistent with the rate of 36.5 ± 10.8 Hz recorded in the parkinsonian macaque (**Figure 8B**, before 100 ms)^{40 45}.

The authors reconstructed the first morphology from a long-tailed macaque (*Macaca fascicularis*) using biotin dextran amine labelling and axonal tracing⁴⁶. The soma of the neuron is in the STN, while its axon finishes in the GPi (**Figure 6**). The original geometry courses dorsally along the ventral border of the thalamus on its way to the GPi. STN projection neurons can also course ventrally along the lateral border of the STN⁴⁶. Thus, the authors created two alternative morphologies based on the initial one (type 3 and type 4, **Figure 6**). Only the original morphology (type 1) was used in this work. To clarify the coming graphs, we have numbered the important sections as follows: soma is section 0, the first node of Ranvier is section 1, the second node is section 2, and so on, until the last node of Ranvier, which is section 28 (**Figure 7**).

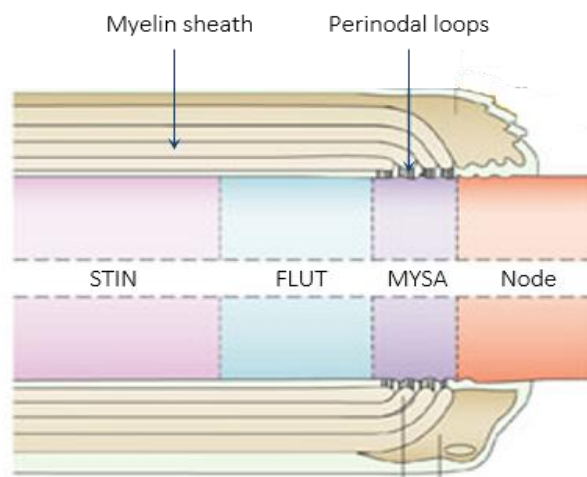


Figure 5 | Types of section across the axon. STIN stands for stereotyped internode, FLUT for fluted region, MYSA for myelin sheath attachment, and node is a node of Ranvier (adapted from Poliak & Peles, 2003⁶⁵).

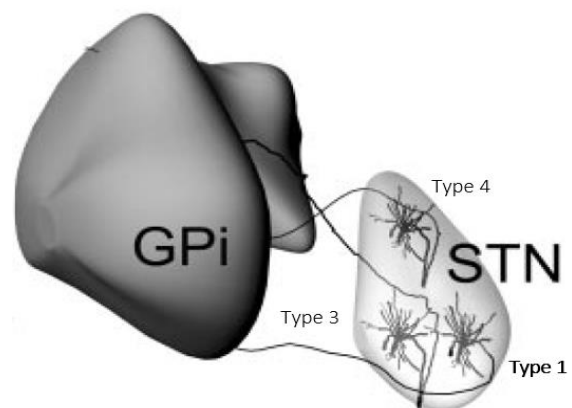


Figure 6 | The three neuron morphologies and their disposition related to the GPi and STN. Only type 1 morphology (in bold) was used in this work (adapted from Miocinovic et al., 2006⁴⁰)

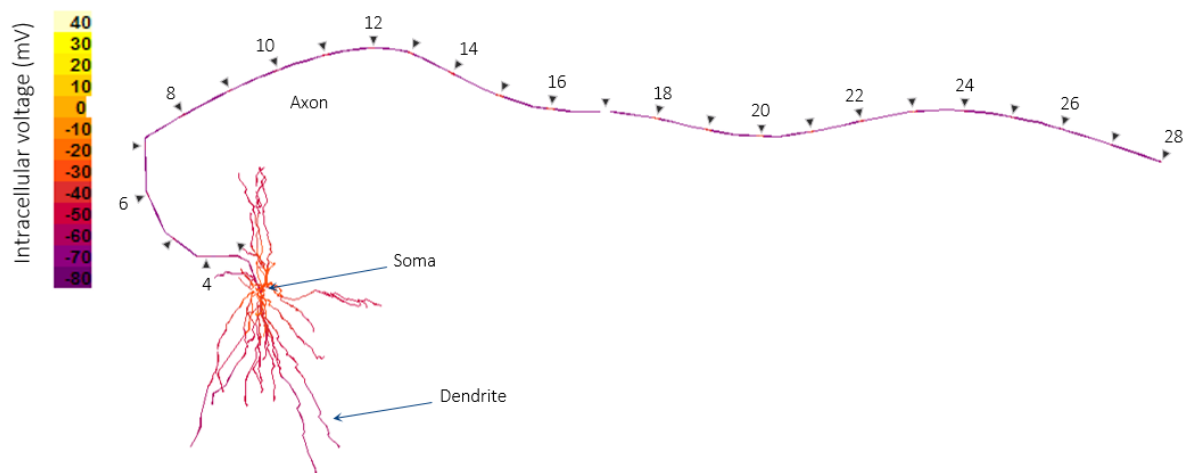


Figure 7 | Representation of the modelled neuron (type 1 morphology) just when it fires a spontaneous somatic AP. Each compartment is coloured according to its intracellular voltage (colour scale on the left). Arrowheads indicate nodes of Ranvier. The numbers are the section numbers used throughout this work: from 0 for the soma to 28 for the last node. The first two nodes are buried in the dendritic tree.

Mechanism files

There are sixteen mechanism files in NMODL language⁴⁰. NMODL is used to add custom mechanisms when the built-in ones are not sufficient²⁷. Mechanisms in NEURON describe biophysical processes that govern electrical and chemical signals. Some examples are voltage-gated ion channels, binding of neurotransmitter to postsynaptic receptors or calcium accumulation. Most of the custom mechanisms present here model ion channels with non-default values or neurotransmitters binding kinetics. Measures have various sources, which are included in the comment section of each *.mod* files.

The model includes a mechanism file describing binding of GABA to the GABA_A receptor. It is used to implement stimulation-induced *trans*-synaptic inhibition by neighbouring neurons. In the same manner than most of the study by Miocinovic et al., 2006⁴⁰, this was omitted in our work. Authors have shown axonal firing is largely unaffected by postsynaptic inhibition⁴⁰ and it may complicate interpretation of our data.

The electric field files

There are thirty electric field files. They specify the extracellular voltage at each neuronal segment when the electrode is delivering continuous 1 V. Each file first establishes a neuronal population of 9–23 cells by X Y Z coordinates and then specifies the voltage of each segment of each neuron.

They all have the same structure, but distinct themselves depending on:

- the morphology file they should work with (there are ten electric field files per STN neuron geometry);

- the polarity setting, i.e. which electrode contact is set as the cathode, and which electrode contact is set as the anode (they all specify electric fields generated during bipolar stimulation);
- the source of the neurons' coordinates, i.e. which electrode was used and how the coordinates of each neuron in the population were obtained (measures from macaque brains or random translations from an initial neuron).

The neuronal populations were not used in this work. Only the first neuron of a type 1 file was tested. Electrode and cell positions of this file originated from two different monkeys (*Macaca mulatta*). Stimulation is bipolar, with the first contact set as the anode and the third as the cathode⁴⁰.

The waveform files

There are four waveform files in the initial model. One waveform file defines one pulse. Waveform, relative amplitude, and pulse duration are all encoded in this file. The waveform files can be interpreted as defining voltage across time, while the electric field files define voltage across space.

More practically, time is discretised into 0.01 ms time steps during simulation. At each time step, the corresponding value in the waveform file is read by NEURON and used as a multiplier of the voltage values contained in the electric field file to compute the voltage at each section of the neuron for any given time. For instance, if simulation is at $t = 1.3 \text{ ms}$, NEURON will read the 130th value of the waveform file. It is, for example, -0.039944 . It will then multiply all values in the electric field file by -0.039944 to obtain the extracellular voltage at each section at $t = 1.3 \text{ ms}$.

The provided waveform files were not used in this work. Instead, ten waveform files were generated in a similar structure by custom MATLAB scripts (see *Waveforms* section hereafter).

The main file

The main file, written in hoc language, is the simulation's orchestra conductor. It plays a multitude of roles, which cannot be exhaustively listed here.

Simulations run in the following way: NEURON first loads the morphology, the electric field and the waveform files specified by the user. It sets simulation and stimulation parameters, initializes the neuron morphology and point processes from the *.mod* files, then runs a threshold seeking algorithm.

Practically, NEURON tests at each trial a series of test pulses. The number of pulses and their frequency are both specified by the user. They were 25 pulses at 136 Hz in our simulations (**Figure 8**).

Finding the action potential threshold

To find the action potential threshold in terms of voltage, the model begins with variables which represent a lower bound and an upper bound. They are initialized at a very high (10 V) and a very low value (0.001 V), respectively. The upper bound represents the voltage which we know is sufficient to evoke APs, while the lower bound represents the voltage which we know is not sufficient. The first trial is run at an amplitude of 1 Vⁱ. If the neuron responds to the stimulation, i.e. at least 80% of the 25 pulses generated an AP, then the amplitude is suprathreshold. In this case, the upper bound is lowered to 1 V, and the next trial is performed at a slightly lower voltage. In the opposite case, i.e. less than 80% of the 25 pulses were followed by an AP, the amplitude is sub-threshold. Therefore, the lower bound is raised to 1 V, and the next trial is performed at a slightly higher voltage. This is performed until the difference between the upper bound and the lower bound is under a precision threshold (called epsilon) specified by the user.

Separating spontaneous APs from stimulation-induced APs

The model differentiates spontaneous APs from stimulation-induced APs by considering a 4 ms time window after the pulse time: if an AP occurs within 4 ms after the test pulse, it is considered stimulation-induced, if it happens outside the 4 ms window, it is considered spontaneous activity.

Final output

The final threshold is set as the upper bound value, as it is the lowest voltage which we know is sufficient to activate the neuron. Finally, NEURON performs a last simulation at the upper bound value, now considered threshold, to record supplementary data such as firing frequencies (not used here). The final data are stored in a text file output at the end of the simulation. This data file is a table of 33 columns and one row per simulation (in our case 65, as for the range of 65 pulse widths we tested per waveform). A log text file is also output by the model. It first contains the simulation and stimulation parameters; then the location of the tested cell(s) (X Y Z coordinates); the times of the 25 pulses; and for each simulation: the APs' output times, defined for each AP as the times at which it is detected at the last node (node 28), the times of the spontaneous APs detected during stimulation, and the times of the APs detected in the soma. All times are in milliseconds at the second decimal.

Simulations

During simulations, time was discretised into fixed 0.01 ms time steps. Backward Euler integration method was used to solve the ODEs that describe the capacitive component and the ionic currents (see *Neuron modelling* section). It is NEURON's default integrator, and is advised for its good qualitative results even with large time steps²⁷. Each simulation run (10 runs; each

ⁱ Voltages are given here as absolute value of the stimulating pulse amplitude. It is positive when stimulation is anodic and negative when stimulation is cathodic.

is a series of 65 successive simulations) took around 13 hours to run on an Asus X550L laptop (Intel ® Core™ i7-4500U CPU @ 1.80 GHz 2.40 GHz, 8.00 Gb RAM, x64-based processor).

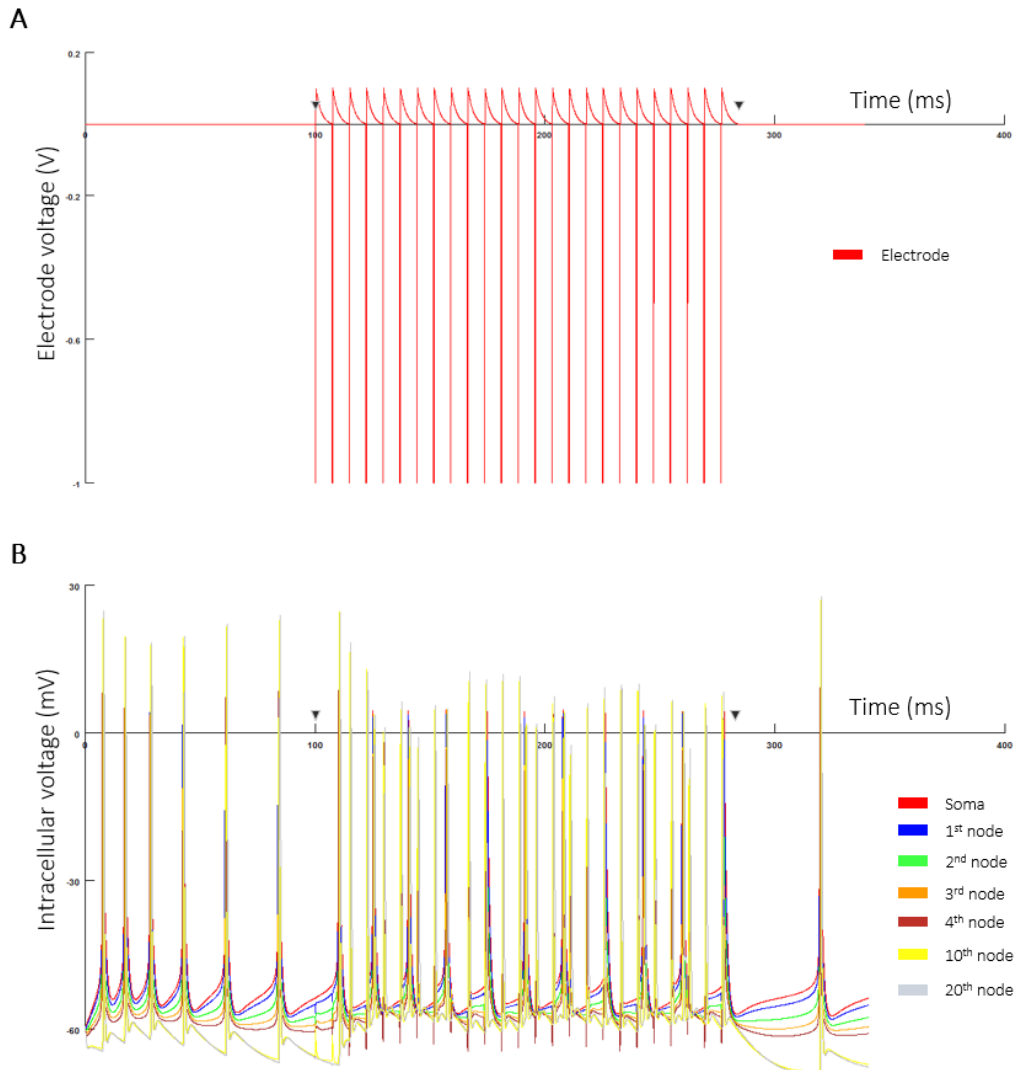


Figure 8 | Snapshot of a simulation. **(A)** Electrode voltage as a function of time (i.e. the DBS pulse shape). The waveform is clinical cathodic, pulse width is 0.2 ms and amplitude is suprathreshold. 25 test pulses are delivered by the electrode at a frequency of 136 Hz. **(B)** Intracellular voltage at various sections across the neuron. Stimulation starts at 100 ms, and finishes around 300 ms (start and end are indicated by arrowheads on the time axes). Before (< 100 ms) and after stimulation (> 300 ms), the neuron is spontaneously firing at a frequency of ~ 32 Hz. The simulation will stop around 400 ms.

Waveforms

The provided waveform files (see *The waveform files* section) were not used in this work. Instead, ten waveforms, among which eight can be considered nonconventional, were generated using custom scripts in MATLAB R2016a. Each were tested in a range of 65 pulse widths ranging from 0.02 ms to 1.3 ms, by 0.02 ms time step. They are represented at the maximum pulse width (1.3 ms) hereafter (**Figure 9**).

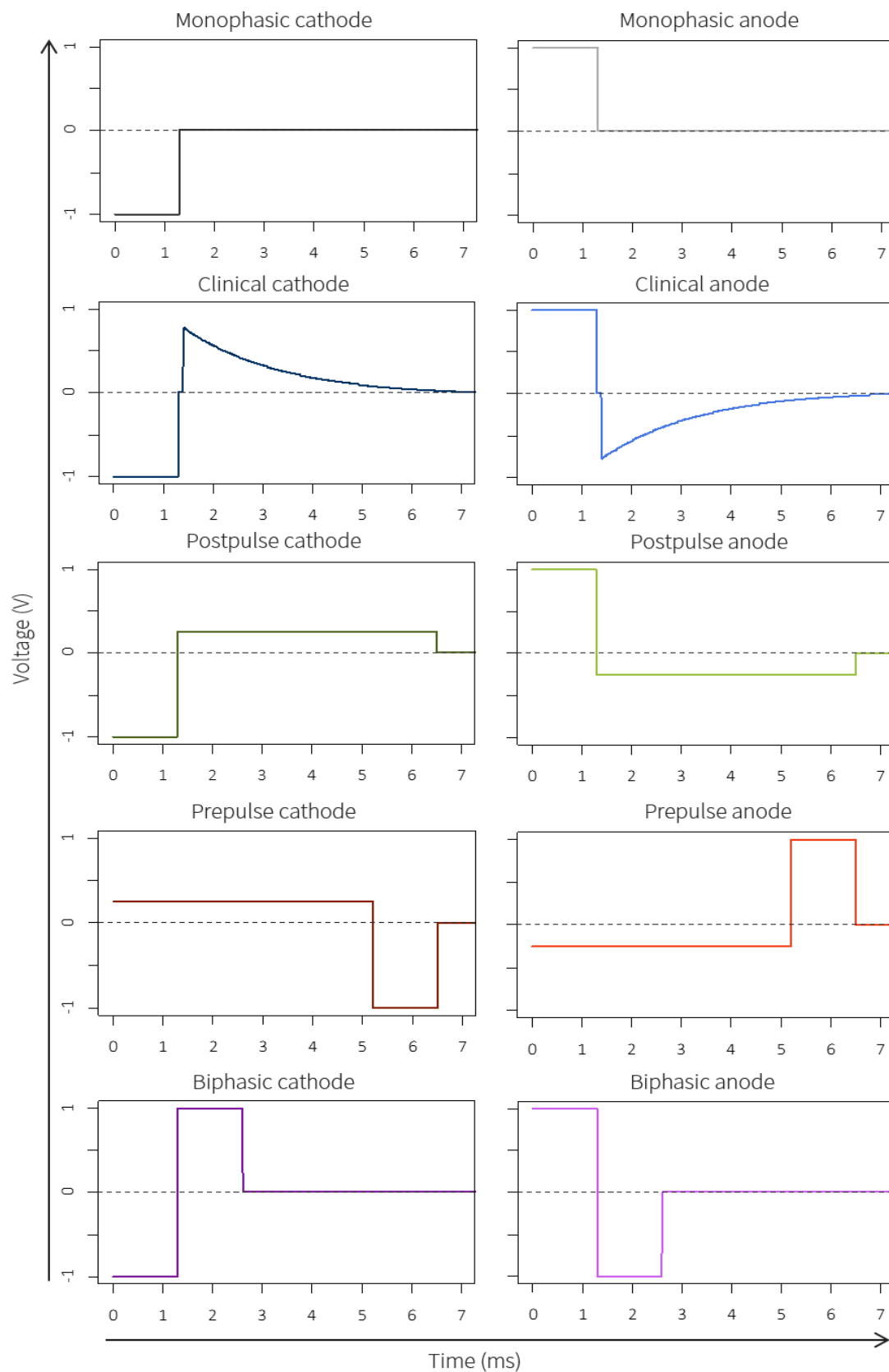


Figure 9 | The ten waveforms used in this study. Cathodic waveforms (cathodic stimulating pulse) are placed in the left column; anodic waveforms (anodic stimulating pulse) are in the right column. Each waveform is represented here by the trace corresponding to the largest pulse width (stimulating phase of 1.3 ms), but is actually tested in a range of 65 pulse widths (from 0.02 to 1.3 ms by 0.02 ms steps).

Development of the model and data processing

All data output by the model were processed with custom scripts in RStudio v.1.0.143.

Explanations

The initial version of the model downloaded from the database contained very few explanations. A first important contribution was thus the addition of detailed comment lines explaining virtually all the workings of the model's main file (see *The main file* section). These should substantially ease future use of the model.

Waveform files

As the initial study⁴⁰ did not test varying parameters in a single run, each waveform file described only one pulse. It was therefore necessary to improve the model in the goal of testing a range of parameters in a single run. After exploring various solutions, we coded a supplementary loop in the core file of the model. By doing so, we were able to readily test a wide range of pulse widths in a single run. In this study, each run consisted in 65 successive simulations, each at a different pulse width. These successive pulses must all be encoded in the waveform file one after the other, i.e. appended to each other. As previously mentioned, one pulse encodes 736 “voltage-multiplier” values, one per time step (0.01 ms). One pulse thus affects voltage during 7.36 ms. Therefore, our waveform files consist in 736×65 values, i.e. 47 840 lines, which are read by successive blocks of 736 values thanks to the added loop. These files can be easily generated with custom MATLAB scripts. The potency of this method, compared to a method that would have allowed the user to choose the range of pulse widths to be tested directly in the main file, is that it would readily function to vary any other parameter during simulation, such as the duration of a gap between the stimulating pulse and the balance of charge (see *Future directions* section). Moreover, the reading of the initial files is unaffected by this modification: the user simply needs to mention in the main script how many pulses the waveform file contains (1 for the initially provided waveforms).

Strength-duration curve

Data points used to plot the strength-duration curves were the thresholds computed by the threshold-seeking algorithm. They are stored in a column of the log file output by the model. When the neuron cannot be stimulated, the model returns a threshold of 10 V. This occurred with all anodic waveforms at the first two pulse widths (0.02–0.04 ms). Thresholds which equal to 10 V are removed before the strength-duration curves are plotted. The rheobase is defined as the threshold at maximum pulse width, i.e. the Y coordinate of the data point further to the right of the strength-duration curve (pulse width = 1.3 ms). The chronaxie is then computed. It is the

pulse width (X coordinate) whose threshold (Y coordinate) is the closest to twice the rheobase. If two successive thresholds are equally close to twice the rheobase, the final chronaxie is set as the average of their pulse widths.

The chronaxie is a universal concept to describe strength-duration curves. We thus included it in our graphs. However, its utility is limited in our situation. Indeed, it is mainly used to compare the excitability of different tissues or structures (see *Strength-duration curve* section), but we tested the same single neuron throughout this study. Moreover, it was historically defined using monophasic, rectangular stimuli. Incidentally, it is unclear if chronaxie is still valid and useful as a measure of excitability when nonconventional waveforms are employed³⁶. Overall, chronaxie measurements are included here mainly for potential future use, for instance comparison between the excitability at various cell locations or of different neuronal morphologies (see *Future directions* section).

A superficial bug existed in the threshold-seeking algorithm (see *The main file* section). By allowing the search to end on a stimulation that was unsuccessful, the algorithm could sometimes return values for the lower bound higher than the final threshold value. Although the threshold value was correct, this small bug did not allow the user to appreciate the distance between the lower and the upper bound, and thus how precise the threshold estimation was. This bug was corrected by preventing the algorithm to end on an unsuccessful stimulation. In these cases, it also increases the precision of the threshold estimation. This situation was fairly uncommon in our setting so should not extend simulation times by much.

Initiation sites bubble graph

We encoded the writing of a supplementary output file which stores the times where an AP was detected at the soma or at any node of Ranvier across the neuron's axon during stimulation. This data is recorded thanks to a built-in NEURON point process called AP counter. It can be placed at any section and will record the times when voltage crosses the threshold value in the upward direction, i.e. when an AP is detected in the region. The output file consists in a table where each row is a section which contains an AP counter. The successive simulations (65 in our case) each produces a table which is appended to the file. The final file thus has *number of AP counters* \times *number of simulations* lines, in our case: $29 \times 65 = 1885$ lines. However, a problem arose as each AP does not necessarily propagate through every section of the neuron. For instance, APs initiated in the axon do not always backpropagate all the way back to the soma (**Figure 10**). When one AP does not propagate through every section of the neuron, all the rows of one column are not filled. However, NEURON will write the times of the next AP in the empty table cells of the previous columns. For example: if the first AP occurring during stimulation does not propagate through section 1 (node 1) the corresponding cell in the table (2nd row, 1st column) will not be filled. If the next AP does propagate through section 1, NEURON will fill this empty cell by this AP's time at section 1. As the simulation runs, this creates cumulative shifts in columns. Eventually, each column of this raw file does not contain times all belonging to the

same AP. Due to how opening and closing files operate in hoc language, we do not believe this problem could be solved at the source. Instead, we wrote a R function that could allocate times to their correct column, i.e. gather all the times belonging to the same AP in a single column. APs take less than 2 ms to propagate through the neuron (**Figure 10**). It thus works by considering a 2 ms window after the AP's initiation time, which corresponds to the minimum time of each aligned column. Times that are within 2 ms after the initiation time are preserved in the column, while times which are larger than *initiation time* + 2 do not belong to the AP and are shifted one column to the right. As the initiation time of the first AP, i.e. the minimum of the first column, is always correct (APs' times which are not in their correct columns can only originate from subsequent APs, thus have larger time values), the function loops from the first to the last column, shifting values to the right when needed. The result is easily confirmed by plotting a sample of the APs' times (**Figure 10**) and by comparing the times in the last row, i.e. last node of the axon, with the APs' output times stored in the log file (see *The main file* section). They are identical ± 0.02 ms. Properly collecting these data was a prerequisite to our study of the APs' initiation sites.

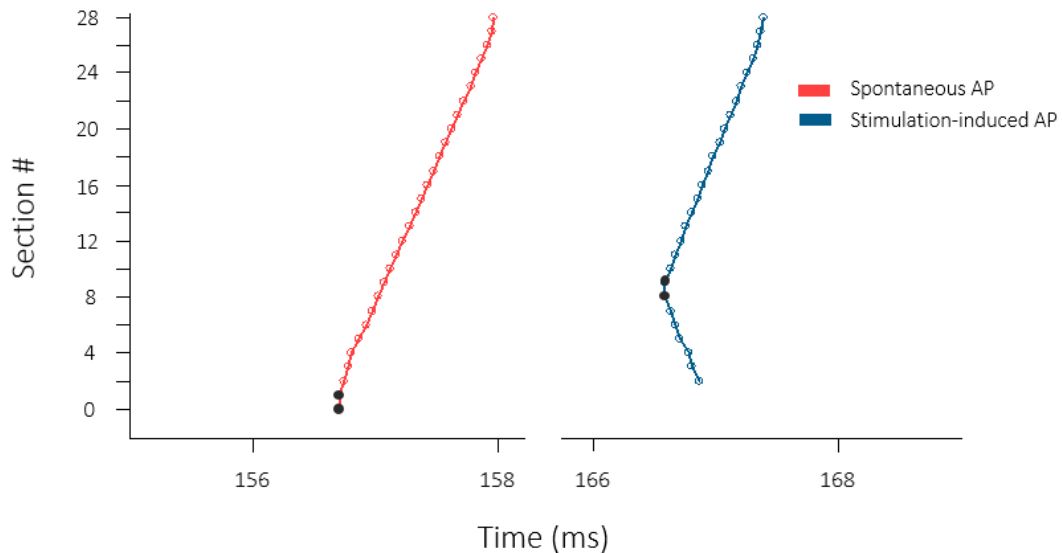


Figure 10 | Propagation of two APs, one spontaneous (in pink) and one stimulation-induced (in blue), through the STN neuron's sections (see **Figure 7** for the section numbers). The initiation sites of each AP correspond to the Y coordinates of the data points with the minimum times (in black). It is section 0 or 1 (soma or 1st node; their times are exactly equal) for the spontaneous AP, and section 8 or 9 (8th or 9th node) for the stimulation-induced AP.

The model produces one time file for each simulation run (65 successive simulations). Succinctly, the R script generating the initiation sites bubble graph works first by splitting this file into its 65 tables, which are stored in a list of matrices. Each table stores the APs' times collected at one pulse width. If the corresponding threshold was 10 V, i.e. the neuron could not be stimulated at this pulse width (see *Strength-duration curve* section), the time matrix is removed from the list. The column-allocating function is then run on each matrix, making use of the *lapply* R function. At this point, each column of each table now corresponds to an AP and each row to a section. The initiation site(s) for each AP are then computed: it corresponds to the row (section) of the minimum time of each column (AP). If two sections both have the minimum time, we defined

the initiation site as the average of these two sections' indexes. The counts of the number of APs initiated at each initiation site at each pulse width are then computed using *melt* from the *reshape2* package⁴⁷, and *group_by* and *count* from the *dplyr* package⁴⁸.

We implemented two possible ways of distinguishing spontaneous and stimulation-induced APs. The first one is the condition used by the model. It considers a 4 ms time frame after the pulse: if the AP occurs within this time frame, it is classified as stimulation-induced; if it happens after, it is classified as spontaneous. This classification method is relatively arbitrary, and caused issues in certain cases (see *Prepulse waveforms* section). Instead, the second method classifies APs based on their initiation site: it is considered stimulation-induced if it is initiated in the axon and spontaneous if it is initiated in the soma. This method is more rational, produces cleaner graphs and works where the first classification fails. Spontaneous APs are indeed fired from the soma, but this method makes the additional assumption that all soma-initiated axons are not stimulation-induced. The original article confirms that this assumption is safe by showing that somatic firing is largely unaffected by extracellular stimulation⁴⁰. Therefore, we chose this classification for the initiation sites bubble graphs included in this work.

Latency times scatter plot

The R script generating the latency times scatter plots takes the log and the time files as input. Briefly, it extracts the times of the 25 test pulses from the log file. It then processes the time file in the same manner than for the initiation sites bubble graph (see *Initiation sites bubble graph* section), eventually computing the initiation time of each AP. APs initiated in the soma are assumed to be spontaneous and are removed. APs which occurred during simulations where the neuron could not be stimulated (threshold = 10 V) are also removed. As each test pulse did not necessarily generate an AP, deltas between pulses and APs cannot simply be computed as the difference between pulses and APs of the same index. Rather, a type of brute-force method is employed: all possible pairwise differences between one initiation time and one pulse time are computed. From this pool of deltas are deleted negative values and values over 7.36 ms, which is the time of one complete waveform (**Figure 9**). What is left from the pool is displayed in a scatter plot as a function of pulse width.

Graphics

Figures 4, 9–15; and supplementary figures 3 and 4 were created with RStudio v.1.0.143⁴⁹. The *ggplot2* package⁵⁰ was used for the initiation sites bubble graphs. Odd pulse numbers (1st, 3rd, 5th, ...) were omitted in the initiation sites graphs and the latency times scatter plots to avoid bubbles superimposition and overplotting, respectively.

Figures 7, 8; and supplementary figures 1, 5 and 6 were generated with NEURON v.7.4³⁰.

Finalisation of the figures, such as addition of labels or creation of the layout, was done with Microsoft PowerPoint 2016.

Results and discussion

Monophasic waveforms serve as control

Monophasic waveforms serve as a preliminary way of testing the model. As they do not provide a balance of charge (**Figure 9**), they would be unsafe *in vivo* and cannot be tested (see *Stimulation parameters* section). They thus mainly constitute a control situation.

The strength-duration curve for monophasic anode is at every point higher than the one for monophasic cathode (**Figure 11A**). This is also reflected by the anodic rheobase which is more than twice the rheobase for cathodic stimulation (1.23049 V vs. 0.542969 V). Chronaxies, on the other hand, are equal for both (0.22 ms).

With regard to the initiation sites, under the cathodic waveform, stimulation-induced APs are consistently generated around section 8 (8th node of Ranvier) (**Figure 11B**); while they are generated from section 14 (14th node of Ranvier) under anodic stimulation (**Figure 11C**).

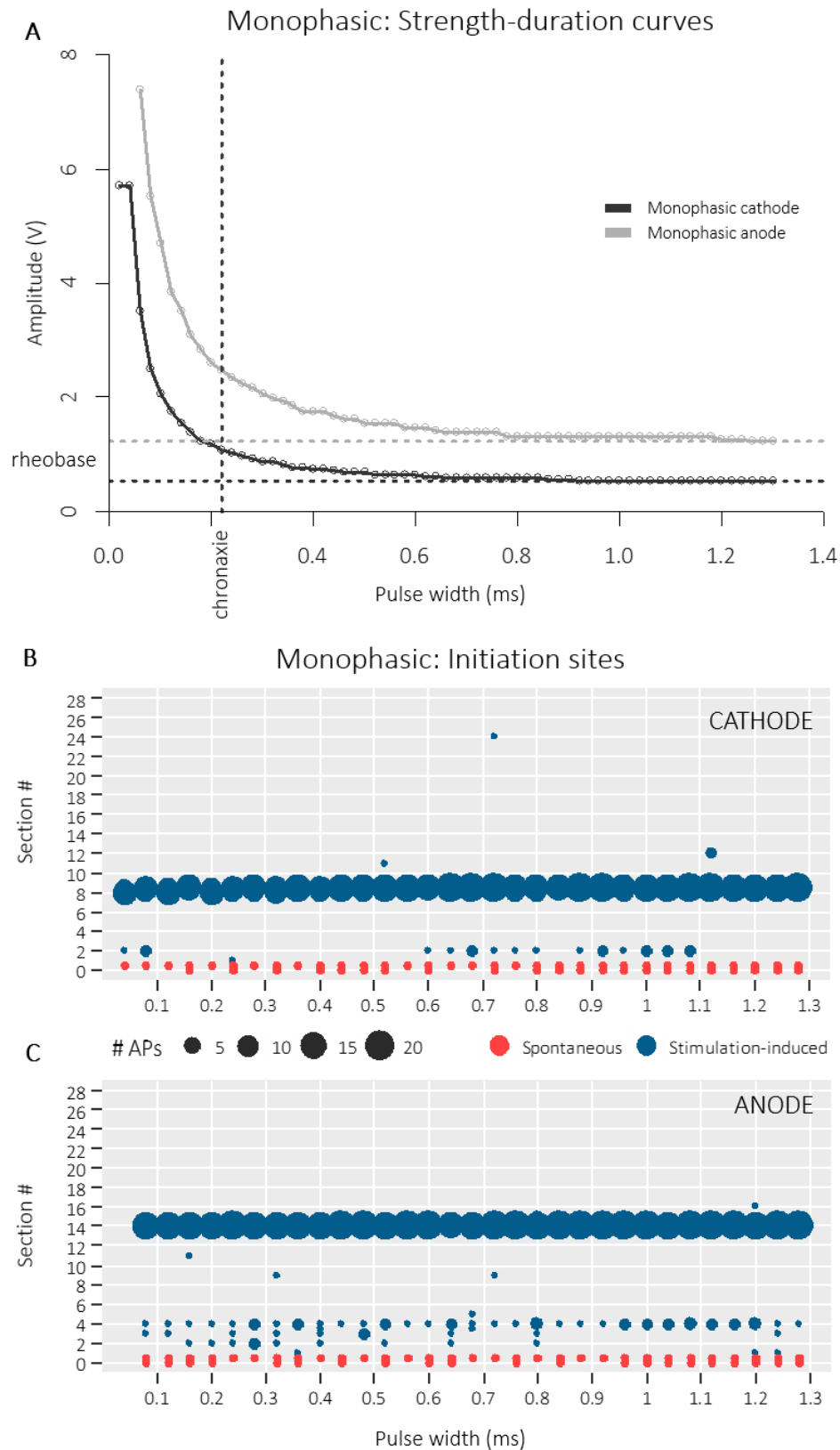


Figure 11 | Stimulation with the monophasic waveforms. **(A)** Strength-duration curves for monophasic cathode (black) and monophasic anode (grey). Monophasic cathode: rheobase = 0.542969 V, chronaxie = 0.22 ms. Monophasic anode: rheobase = 1.23049 V, chronaxie = 0.22 ms. **(B)** APs' initiation sites under monophasic cathode. **(C)** APs' initiation sites under monophasic anode. The area of each bubble is proportional to the number of APs fired at the section. Pink bubbles correspond to spontaneous APs, blue to stimulation-induced APs.

Cathodic stimulation can be explained by the properties of the voltage-gated sodium channels. The sodium channel has two gates: the activation gate and the inactivation gate. Each is modelled by a variable: an increase in the value of m represents activation gate opening; while an increase in the value of h represents inactivation gate opening (see *Neuron modelling* section). At rest, the voltage-gated sodium channel is closed by the activation gate: m is low. h , however, is almost entirely open with a value around 0.8. Time constants of the activation gate and the inactivation gate differ by two orders of magnitude. Stated differently, the activation gate can respond a hundred times faster to increases in transmembrane potential than can the inactivation gate. By delivering a stimulus of negative voltage, the compartment closest to the electrode gets depolarised, i.e. intracellular voltage rises. In response to membrane depolarisation, voltage-gated sodium channels open, which is modelled by an increase in the value of m . It allows sodium ions to flow down their concentration and potential gradients, which is from the extracellular to the intracellular compartment (at rest, sodium ion concentration is higher extracellularly). This creates a cascade reaction: further depolarisation causes further opening of sodium channels, i.e. further increase in the value of m . Simultaneously, but at a much slower rate, the sodium channel inactivation gate begins to close, which is modelled by a decrease in the value of h . Overall, an increase in membrane potential has the dual, conflicting effect of both increasing and decreasing membrane conductance. However, these changes do not occur simultaneously thanks to the difference in the time constants. As closure of the inactivation gate continues, sodium influx slows down and eventually stops. With the help of efflux of potassium cations through voltage-gated potassium channels, membrane potential repolarises and returns to equilibrium²⁴.

Anodic stimulation, on the other hand, is less intuitive. As first approximation, it can be explained by an electrophysiological phenomenon called anodic break excitation, which can also be described in terms of voltage-gated sodium channels dynamics. Anodic stimulation hyperpolarises the membrane, i.e. decreases intracellular voltage. At the end of a long (or alternatively, very strong) anodic pulse, the inactivation gate is entirely open, i.e. $h \simeq 1$, and the activation gate is closed, i.e. $m \simeq 0$. As soon as the pulse is finished, intracellular voltage rises back to its initial value. The inactivation gate remains open for a while because of its slow time constant. The activation gate, on the other hand, is fast to react and thus opens rapidly to move back to its rest position (m increases). During this time window when activation gate rapidly opens and inactivation gate is still opened from hyperpolarisation, sodium ions flow into the cell. This influx causes membrane depolarisation, which can be sufficient to reach threshold and generate an AP²⁴.

This difference in mechanism between cathodic and anodic stimulation is well illustrated by the strength-duration curves (**Figure 11A**): for equal pulse widths, anodic stimulation must be stronger (i.e. of higher amplitude) to activate the neuron; alternatively, for equal amplitudes, anodic stimulation must be longer (i.e. of larger pulse width). Moreover, the neuron cannot be stimulated at very short pulse widths (under 0.06 ms) using anodic stimulation (see *Strength-*

duration curve section). Indeed, a too weak or too short pulse seems to be insufficient to completely open the inactivation gate, i.e. to bring h value close to 1, and to completely close the activation gate, i.e. to bring m value close to 0, which are the conditions to trigger anodic break excitation. Overall, cathodic stimulation is thus more efficient. Larger pulse width or amplitude, and thus more energy per pulse, are necessary to stimulate the neuron in the anodic setting, which would drain the device's battery more rapidly.

Alternatively, anodic stimulation can also be described in more electrical terms by Kirchhoff's current law (see *Neuron modelling* section). When stimulation is cathodic, i.e. electrode's voltage is negative, current leaves the neuron to reach the electrode. It does so by the closest node of Ranvier. However, Kirchhoff's current law states that the sum of currents leaving a section must be equal to the sum of currents entering the section. Thus, current must enter the neighbouring sections to compensate for this loss. Voltage thus decreases at these nodes to allow current to pour in, which means they get hyperpolarised. When stimulation is anodic, i.e. the electrode's voltage is positive, the opposite phenomenon takes place. Current enters by the node closest to the electrode. Thus, current must leave from neighbouring sections to compensate. Voltage increases in these sections to allow current to pour out, so these nodes are now depolarised. If the stimulus is particularly long and/or strong, voltage at these neighbouring nodes can reach threshold, in such case an AP is fired⁵¹. This phenomenon seems to explain the difference in initiation sites (**Figure 11BC**). APs are fired from the 8th node under cathodic stimulation, which seems to be the closest node to the electrode (**Supplementary Figure 1**). This node should be the main node from which current pours out during anodic stimulation, and into which current pours in during anodic stimulation. Therefore, we would expect firing of APs from nodes downstream (further from the soma) and upstream (closer to the soma) node 8 during anodic stimulation. Coincidentally, this is what we observe: under anodic stimulation, most APs are fired downstream at node 14, and a few are fired upstream around node 4. As to why fewer APs are fired closer to the soma, it may be explained by recurrent hyperpolarisation caused by the spontaneous APs. Geometric considerations, such as distance and orientation relative to the electrode, also play a role to why node 14 and 4 specifically fire more APs than the others.

The recharge phase of the clinical anodic waveform is not passive at long pulse widths

In vivo, the stimulating pulse must be accompanied by a recharge phase which provides the balance of charge. Typically, the stimulating pulse is cathodic and is directly followed by the anodic recharge phase (**Figure 4**). The goal of this phase is to reverse electrochemical reactions that may have happened around the electrode but not to stimulate the neuron (see *Stimulation parameters* section). Anodic break excitation, while it is desired during anodic stimulation, can thus become troublesome if it occurs during the recharge phase. Clinical waveforms have been developed to prevent this⁵². The balance of charge slowly decays to 0, which should allow the inactivation gate to return to its partially closed rest level without generating an AP²⁴.

Like monophasic waveforms, the strength-duration curve for clinical anode is at every point higher than the one for clinical cathode (**Figure 12A**). This is reflected by the anodic rheobase which is slightly larger than the cathodic one (0.542969 V for cathode vs. 0.814453 V for anode); and the anodic chronaxie, which is more than double the cathodic one (0.22 ms for cathode vs. 0.47 ms for anode). Moreover, the strength-duration curve for clinical cathode is virtually identical to the one for monophasic cathode. This is confirmed when superimposed (**Supplementary Figure 2**) and by the rheobases and the chronaxies which are identical. The strength-duration curve for clinical anode is also identical to its monophasic counterpart, except for pulse widths over 0.9 ms where the clinical anodic waveform decreases more than the monophasic one. The maximum deviation is at maximum pulse width, where it is given by the difference between the rheobases: $1.23049 - 0.814453 = 0.476037$ V. Initiation sites for clinical cathode are also virtually identical to its monophasic counterpart, the most common initiation site being node 8 (**Figure 12B**). For anodic waveforms, they are similar until around 1.0 ms pulse width, where the most common initiation site for clinical anode drops from node 14 to node 8 (**Figure 12C**).

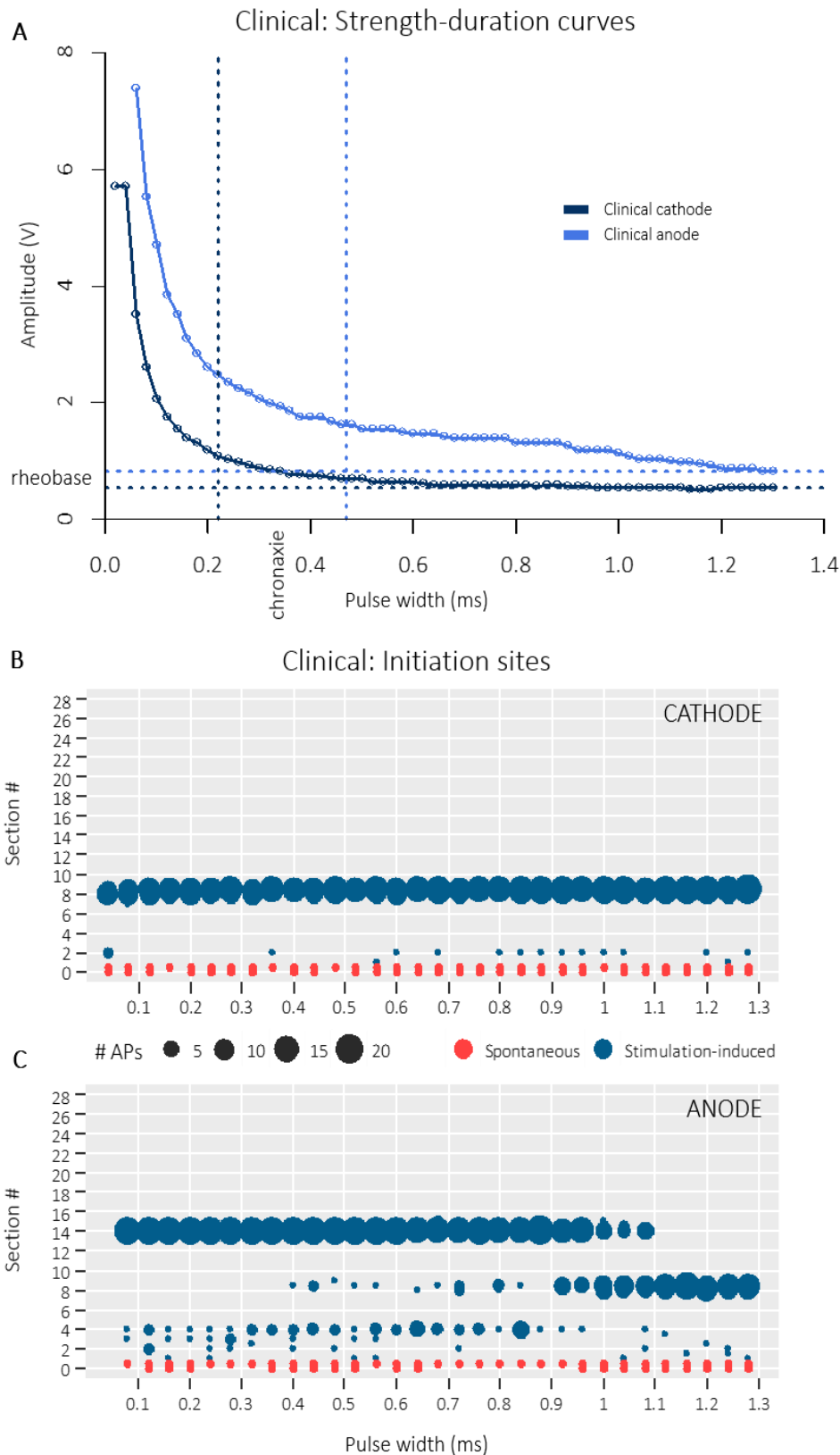


Figure 12 | Stimulation with the clinical waveforms. **(A)** Strength-duration curves for clinical cathode (dark blue) and clinical anode (light blue). Clinical cathode: rheobase = 0.542969 V, chronaxie = 0.22 ms. Clinical anode: rheobase = 0.814453 V, chronaxie = 0.47 ms. **(B)** APs' initiation sites under clinical cathode. **(C)** APs' initiation sites under clinical anode. The area of each bubble is proportional to the number of APs fired at the section. Pink bubbles correspond to spontaneous APs, blue to stimulation-induced APs.

The overall similarity in the results at short pulse widths (under approximately 0.9 ms) between monophasic and clinical waveforms confirms that the recharge phase, thanks to its slowly decaying component, does not affect stimulation. Only the stimulating pulse causes the neuron to fire APs at these pulse widths. Therefore, explanations for the strength-duration curves and the initiation sites are analogue to those for monophasic waveforms. Notably, clinical anodic stimulation is also inefficient to activate the neuron compared to the cathodic stimulation. The effect even seems emphasised here, as reflected by the larger difference between anodic and cathodic chronaxies and rheobases. It should however be noted that the range of pulse widths tested may be too narrow to allow the anodic strength-duration curve to reach rheobase. It may be that rheobases get closer to one another at longer pulse widths, which would have the effect of pulling chronaxies further apart.

Over 0.9 ms pulse width, results for the anodic waveform differ. At these durations, the cathodic recharge phase, which is approximately four times longer than the stimulating pulse, i.e. more than 3.6 ms long (**Figure 9**), seems to be long enough to affect stimulation. The first piece of evidence for this interpretation is the initiation site: it drops to the 8th node, which is typical of cathodic stimulation (**Figure 11B**). To confirm this intuition, we plotted the firing latency times for the clinical anodic waveform, i.e. the deltas between the very start of each pulse and the firing of an AP (see *Latency times scatter plot* section). What we observed is a clear rise in latency times around 0.9 ms pulse width (**Supplementary Figure 3**). The picture seems slightly more complex than expected though. While it is certain that the recharge phase is responsible for this switch in initiation sites (otherwise we would be in the more trivial situation of the monophasic anode), we would expect a bigger rise in latency times if the node 8 APs were fired at the very end of the long recharge phase. For pulse widths over 0.9 ms we would expect latency times around $pulse\ width + recharge\ phase \geq 4.5\ ms$. Notwithstanding, the answer probably lies in the effects of the previous pulses. Each stimulation consists in a series of 25 pulses; the recharge phases of the previous pulses may thus have consequences on the effects of the successive ones. The long cathodic recharge phase has the effect of hyperpolarising node 14 and node 4, which decreases their propensity to fire APs during the next anodic stimulating pulse. It also depolarises node 8. Although it is apparently not sufficient to generate an AP as such, depolarisation at node 8 may build up by the addition of successive cathodic recharge phases. This effect can even be emphasized by the decrease in the interpulse interval: as pulse width increases, the recharge phase is gradually eroding the periods with null voltage between pulses. Eventually, APs could be fired from node 8. This is not taking into account the strong anodic stimulating pulses which should counteract these effects. As seen with the monophasic waveforms, to equally raise intracellular voltage, more charge must be injected when stimulation is anodic than when stimulation is cathodic. The effect should be exactly opposite if the goal is to lower intracellular voltage. As both phases inject the same amount of charge here, it makes sense that the charge delivered during the anodic pulse is not sufficient to lower node 8 voltage back to rest value after it has been raised by the cathodic recharge phase. Successive

cathodic recharge phases may thus progressively rise depolarisation until APs are fired from node 8. The progression of node 8 and node 14 intracellular voltage as a function of time at short and long pulse width seems to confirm this explanation (**Supplementary Figure 5**). Finally, this effect is not observed with the cathodic clinical waveform. As we saw with monophasic waveforms, anodic stimulation must be stronger to activate the neuron. This would explain why the anodic recharge phase of the cathodic clinical waveform is insufficient to generate APs, while the cathodic recharge phase of the anodic clinical waveform is.

Whatever the exact mechanism, the main observation here is that at long pulse widths, the cathodic recharge phase of the clinical anodic waveform is not passive anymore. It affects stimulation, causing a decline in the strength-duration curve and a switch in initiation sites. If this effect is problematic, a potential solution suggested by the computational model would be to slightly overshoot the charge delivered by the anodic stimulating pulse at long pulse widths. This should bring back node 8's voltage to its rest value at each pulse, preventing the successive cathodic recharge phases to cause cumulative depolarisation. The overall goal would be to balance the downstream effects on intracellular voltage, and not necessarily the injected charge.

At short pulse widths, the anodic postpulse waveform moves the initiation site without affecting the strength-duration curve

Compared to clinical waveforms, the particularity of the postpulse waveforms is to have a rectangular recharge phase (**Figure 9**).

The strength-duration curves for postpulse waveforms (**Figure 13A**) are virtually identical to those of monophasic waveforms (**Figure 11A**). This is particularly striking when superimposed (**Supplementary Figure 2**), and is reflected by the chronaxies and rheobases which are practically equal (cathodic rheobases: 0.515625 vs. 0.542969 V; cathodic chronaxies: 0.24 vs. 0.22 ms; anodic rheobases: 1.171875 vs. 1.23049 V; anodic chronaxies: 0.21 vs. 0.22 ms; respectively postpulse vs. monophasic waveform). Initiation sites for postpulse cathode are also like its monophasic counterpart, the most common being node 8 (**Figure 13B**). Initiation sites for postpulse anode are slightly different. At very short pulse widths (under 0.2 ms), the most common initiation site for stimulation-induced APs is node 8, but it switches rapidly to node 14 (and 4 to a lesser extent) as pulse width increases (**Figure 13C**).

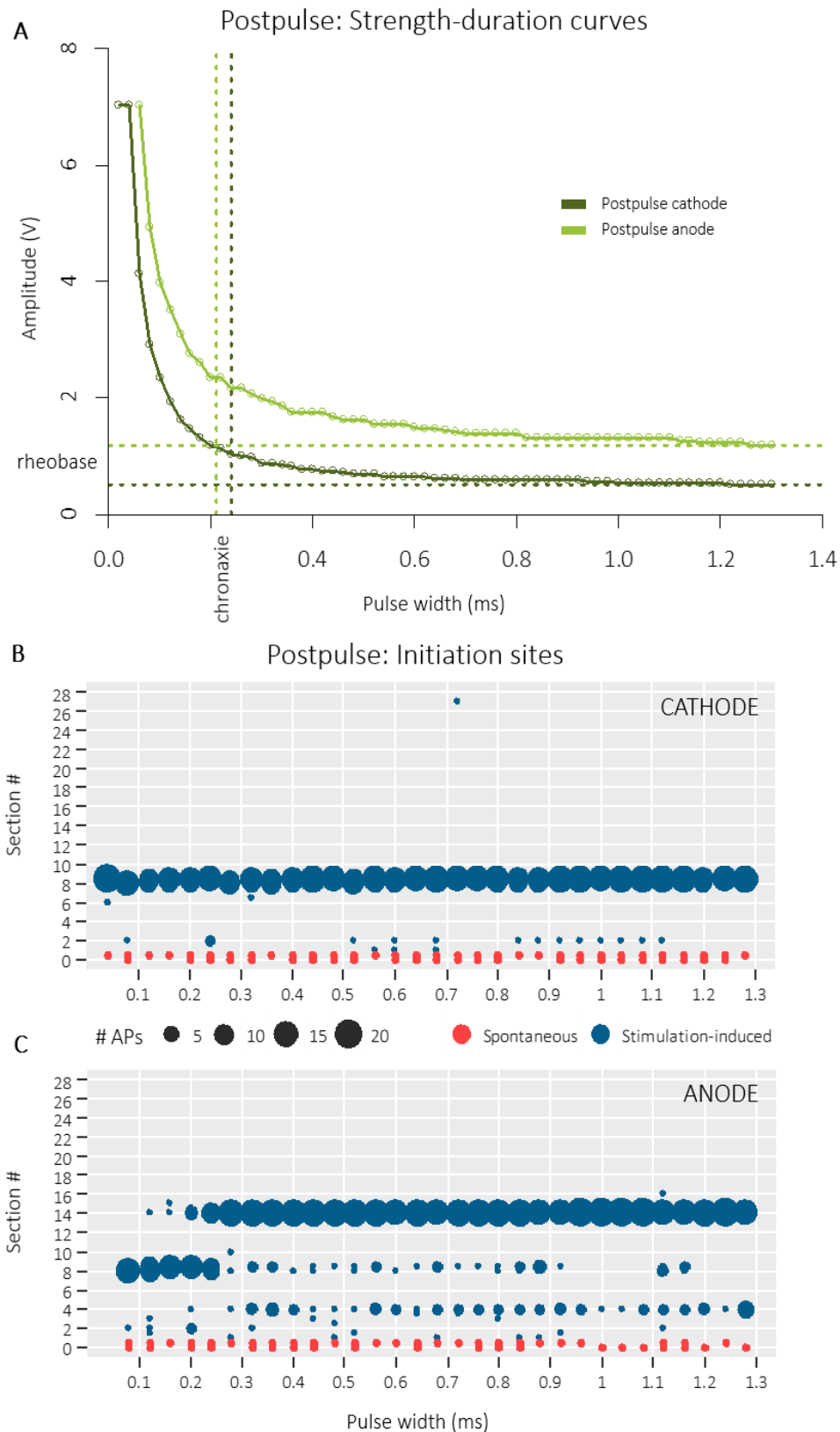


Figure 13 | Stimulation with the postpulse waveforms. **(A)** Strength-duration curves for postpulse cathode (dark green) and postpulse anode (light green). Postpulse cathode: rheobase = 0.515625 V, chronaxie = 0.24 ms. Postpulse anode: rheobase = 1.171875 V, chronaxie = 0.21 ms. **(B)** APs' initiation sites under postpulse cathode. **(C)** APs' initiation sites under postpulse anode. The area of each bubble is proportional to the number of APs fired at the section. Pink bubbles correspond to spontaneous APs, blue to stimulation-induced APs.

Similarly to clinical waveforms (except at long pulse widths), the strong similarity between postpulse and monophasic waveforms' strength-duration curves indicates that the recharge phase does not affect the efficiency of stimulation: a similar strength is necessary to stimulate the neuron, whether the recharge phase is present or not. Except at long pulse widths, the strength-duration curves are also alike those for clinical waveforms. This demonstrates that the shape of the recharge phase, whether it is an exponential decay or a rectangle, does not have a significant effect on the strength-duration curves. As first approximation, efficiency should thus not be affected by the shape of the recharge phase.

Despite noticeable differences in the strength-duration curves, initiation sites do vary for the postpulse anodic waveform: at short pulse widths (under 0.2 ms), the most common initiation site is node 8, which is expected of cathodic stimulation. In the same manner than for clinical waveforms, we plotted latency times to get some insights (**Supplementary Figure 3**). A similar effect is observed in both cases: latency times seem slightly longer than the pulse width when APs are fired predominantly from node 8. However, this effect occurs at short pulse widths here. This is particularly hard to explain as the short recharge phase (maximum 0.8 ms when pulse width is 0.2 ms) is not expected to have any effect on stimulation and the gap at null voltage between successive pulses should be sufficiently long to allow intracellular voltages to return to rest values. A suggestion may be a phenomenon analogue to anodic break excitation occurring at node 8 because of the instantaneous switch from anodic to cathodic voltage (**Figure 9**). At the end of the short anodic stimulating pulse, the activation gate of the voltage-gated sodium channel, m , should be close to 0 as it is both already low at rest and fast to react. The inactivation gate h is probably too slow to react to the short pulse and would thus remain at rest value, which is around 0.8, i.e. almost entirely open. In the few moments after the switch from anodic to cathodic voltage, m would quickly open while h would remain in its open state. With strong amplitude, this may be sufficient to allow the influx of enough sodium ions to evoke an AP. Although the recharge phase of the clinical anodic waveform is stronger initially, this phenomenon would not occur because it almost instantaneously decays, not allowing the activation gate m to remain open for long enough while h is still open. This would stop occurring at longer pulse widths because an AP is fired from node 14 or 4 before the switch in voltage.

This effect is interesting as a potential way to gain control over initiation sites at short pulse widths, and without affecting the strength-duration curve.

The prepulse anodic waveform may be useful to double the firing rate at minimum energy cost

Prepulse waveforms are the reversed-order versions of the postpulse waveforms: the rectangular recharge phase occurs before the stimulating pulse. Pulse width and voltage still describe the stimulating pulse, which is the second phase in this case. Theoretically, the recharge phase should provide as adequate balance of charge as if it was after the stimulating pulse²⁵. However, to our knowledge, reversed-order waveforms have never been tested *in vivo*.

Prepulse simulations uncovered a limitation of the model that was not spotted earlier. Indeed, to distinguish between spontaneous and stimulation-induced APs, the model considers a 4 ms time frame after the pulse: if the AP is fired within this time frame, it is considered stimulation-induced; if it is outside, it is considered spontaneous. In prepulse waveforms, the recharge phase, which generally does not trigger APs, precedes the stimulating pulse. Hence, the 4 ms time frame starts counting at the very beginning of the recharge phase. This does not cause problems at very short pulse widths, where the time window remains sufficiently long to detect stimulation-induced APs. However, it quickly causes a problem at medium-length pulse widths (around 0.6 ms). It is easy to understand why: at 0.6 ms, the stimulating pulse will end at *recharge phase + pulse width* = $0.6 \times 4 + 0.6 = 3 \text{ ms}$ after the very start of the simulation. The actual time frame left for a stimulation-induced AP to be considered as such is thus 1 ms. Therefore, quickly after 0.6 ms pulse width, stimulation-induced APs will start to be fired outside the 4 ms time frame, and thus be wrongly classified as spontaneous. Not counting enough APs, the model will react by increasing amplitude until the recharge phase fires APs on its own, which indeed get classified as stimulation-induced as they happen within the time frame. Increasing the time frame duration by 1 or 2 ms only pushes the problem to longer pulse widths. Eventually, we ran the prepulse waveforms simulations with a time frame set as 7.35 ms, which corresponds to the length of the entire pulse. Stated differently, every AP happening during stimulation will be classified as stimulation-induced, even if it is actually spontaneous. Spontaneous APs being very consistent and largely unaffected by extracellular stimulation⁴⁰, the long time frame should not qualitatively change the strength-duration curves. The only risk is a small underestimation of the thresholds: as the model counts the few spontaneous APs as stimulation-induced, a slightly weaker amplitude is sufficient to reach the minimum number of APs.

When superimposed (**Supplementary Figure 2**), prepulse strength-duration curves are very similar to their monophasic counterparts. The main difference seems to be at short pulse widths (under 0.2 ms). Under 0.06 ms, anodic stimulation cannot activate the neuron, which was the case with all previous anodic waveforms. Moreover, at the shortest pulse widths (0.02–0.04 ms for cathode, 0.06 ms for anode), thresholds with the prepulse cathodic waveform are higher than those with the monophasic cathodic one. The effect seems to be opposite with anodic waveforms: thresholds with prepulse waveform are slightly higher at minimum pulse width (**Figure 14A**). Rheobases and chronaxies are very close to the monophasic ones: prepulse

rheobases are less than 10% lower than with monophasic waveforms, and cathodic and anodic chronaxies are slightly higher and lower, respectively (cathodic rheobases: 0.495117 vs. 0.542969 V; cathodic chronaxies: 0.28 vs. 0.22 ms; anodic rheobases: 1.171875 vs. 1.23049 V; anodic chronaxies: 0.20 vs. 0.22 ms; respectively postpulse vs. monophasic waveform). The most common initiation site for prepulse cathode is constant as a function of pulse width, with node 8 as the preferred firing site (**Figure 14B**). For prepulse anode, the most common initiation sites switch from node 8 and some other, inconsistent downstream nodes to mainly node 14 around 0.3 ms pulse width (**Figure 14C**). This phenomenon is very similar to what was observed with the postpulse anodic waveform (**Figure 13C**).

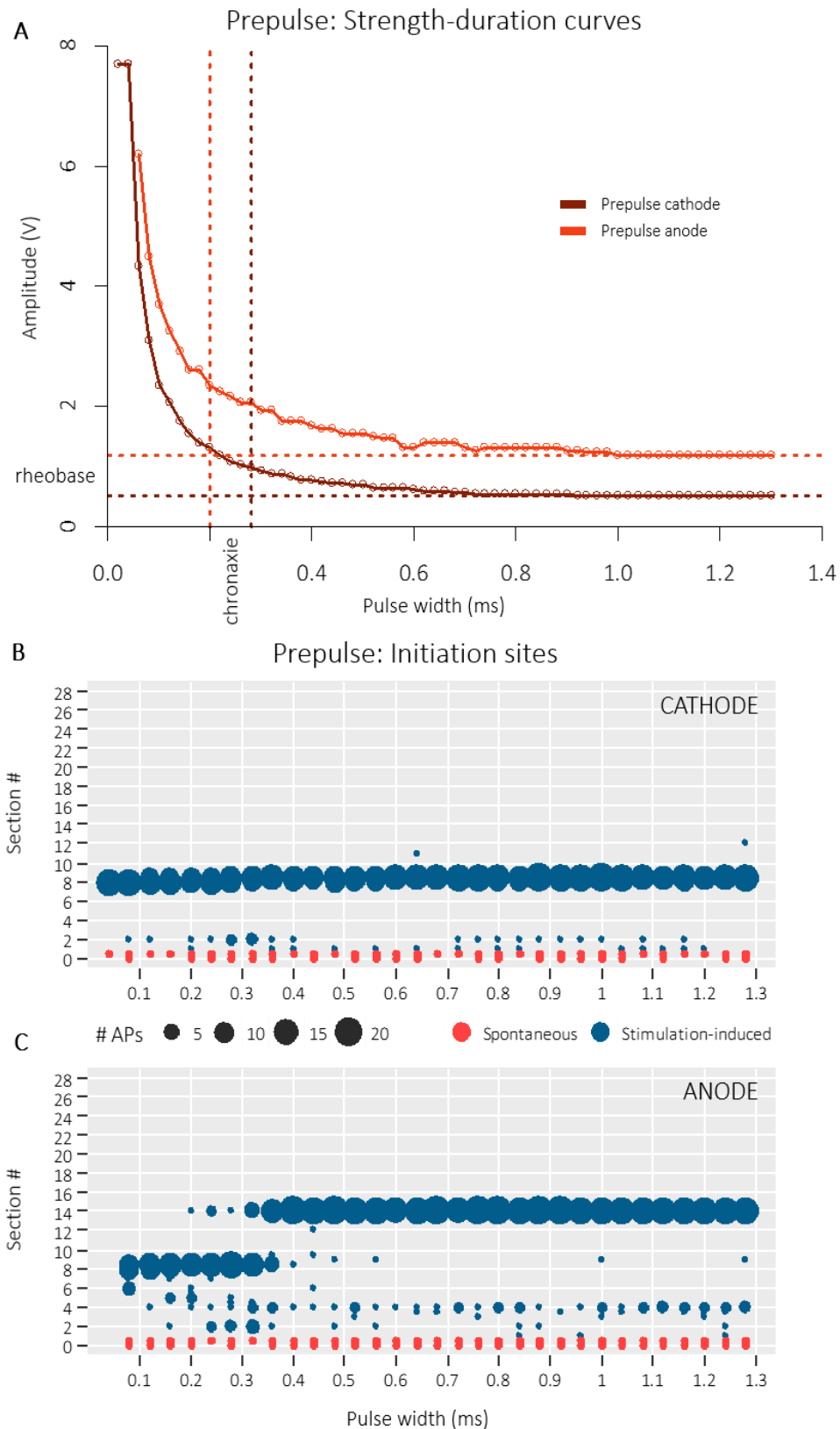


Figure 14 | Stimulation with the prepulse waveforms. **(A)** Strength-duration curves for prepulse cathode (dark red) and prepulse anode (light red). Prepulse cathode: rheobase = 0.495117 V, chronaxie = 0.28 ms. Prepulse anode: rheobase = 1.171875 V, chronaxie = 0.20 ms. **(B)** APs' initiation sites under prepulse cathode. **(C)** APs' initiation sites under prepulse anode. The area of each bubble is proportional to the number of APs fired at the section. Pink bubbles correspond to spontaneous APs, blue to stimulation-induced APs.

In both cathodic and anodic settings, node 8 is the preferred firing site at short pulse widths. This explains the difference in thresholds at the minimum pulse widths. With prepulse cathode, the anodic recharge phase first hyperpolarises node 8, a stronger stimulating pulse is thus necessary next to pull voltage to threshold value and generate an AP. It is the opposite with prepulse anode: the recharge phase first depolarises node 8, a weaker pulse is thus sufficient afterward to generate an AP.

Except for this difference in the strength-duration curve, stimulation with the cathodic waveform is practically unaffected by the anodic recharge phase. Indeed, node 8 stays the most common firing site at every pulse width. This is also confirmed by the latency times (**Supplementary Figure 4**) which steadily increase. This is indeed expected as the latency times measure the delay between the very beginning of the recharge phase and the firing of an AP, and thus include the recharge phase. Explained in mathematical terms, as the recharge phase lasts four times the pulse width, and the APs occur at the very end of the stimulating pulse (so one pulse width after the end of the recharge phase), the equation of the latency times line is given by:

$$y = 4x + x = 5x$$

where y is the latency time and x is the pulse width.

The slope of the latency times line is thus expected to be around 5, which is what we observe in the scatter plot. The length of the recharge phase could also be subtracted from the latencies, in which case we would obtain a scatter plot like monophasic cathode.

Before ~ 0.3 ms pulse width, the most common initiation site for the prepulse anodic waveform is node 8, which is typical of cathodic stimulation. Therefore, we suspect the cathodic recharge phase of generating APs at these pulse widths. This seems to be confirmed by the latency times which fall during the recharge phase (**Supplementary Figure 4**). For instance, at 0.1 ms pulse width, the recharge phase lasts 0.4 ms. Yet, the latency time is around 0.4 ms. APs thus seem to be fired toward the end of the recharge phase (0.1 ms before the end). The recharge phase being cathodic, node 8 is the most common firing site. Node 8, for some geometric reasons such as its proximity or alignment with the electrode (**Supplementary Figure 1**), seems to be particularly prone to activation. Yet, cathodic stimulation is easier to achieve compared to anodic stimulation, in the sense that it needs significantly less pulse width or amplitude to generate APs. These two factors add up to explain why the weak cathodic recharge phase may be sufficient to drive node 8 to fire. The monophasic cathodic waveform seems to confirm this. For instance, at 0.4 ms pulse width, the threshold is ~ 0.74 V. Stated differently, 0.4 ms at 0.74 V are sufficient to activate node 8. For the prepulse anodic waveform, the cathodic recharge phase is 0.4 ms when pulse width is 0.1 ms. At this pulse width, threshold is ~ 3.69 V, so amplitude of the recharge phase is $3.69/4 \approx 0.92$ V. As we have just seen, 0.4 ms at 0.92 V are sufficient to activate node 8. As it occurs before the stimulating pulse, the AP is fired and the axon is hyperpolarised at the

end of the recharge phase, preventing the stimulating pulse from having an effect on node 14 and 4. After ~ 0.3 ms, latency times increase with a slope around 5 like during cathodic stimulation. APs are thus fired at the end of the stimulating pulse as expected. The question remains as to why a switch happens if a cathodic recharge phase as short as 0.4 ms is sufficient to generate APs. This is challenging to explain. It may be caused by the reduction of the gap phase: as pulse width increase, the gap with null voltage between successive pulses is reduced. The axon may thus still be hyperpolarised when the next recharge phase arrives. This would prevent the recharge phase from having the effect it has at short pulse widths, but the stimulating pulse a few milliseconds later would be strong enough to generate an AP, which would be fired from node 14 or 4 as it is anodic.

More interestingly, it seems that the prepulse anodic waveform could be used slightly suprathreshold to evoke two successive APs per pulse (**Figure 15**). When the neuron was stimulated with long pulse widths (1.28 ms) at threshold amplitude (1.171875 V), it fired 23 stimulation-induced APs and 6 spontaneous ones. Slightly over threshold (1.875 V), it fired 47 APs, i.e. almost 2 APs per pulse. For each pulse, one AP seems to be fired from node 8 and another one from node 14. This would be expected if both the cathodic recharge phase is long enough to evoke an AP from node 8 and the stimulating pulse strong enough to evoke an AP from node 14. These results would be particularly interesting to double the firing rate while only slightly increasing energy consumption. Nonetheless, these results remain preliminary and will need to be further investigated.

Prepulse anode: node 8 & node 14 vs. time

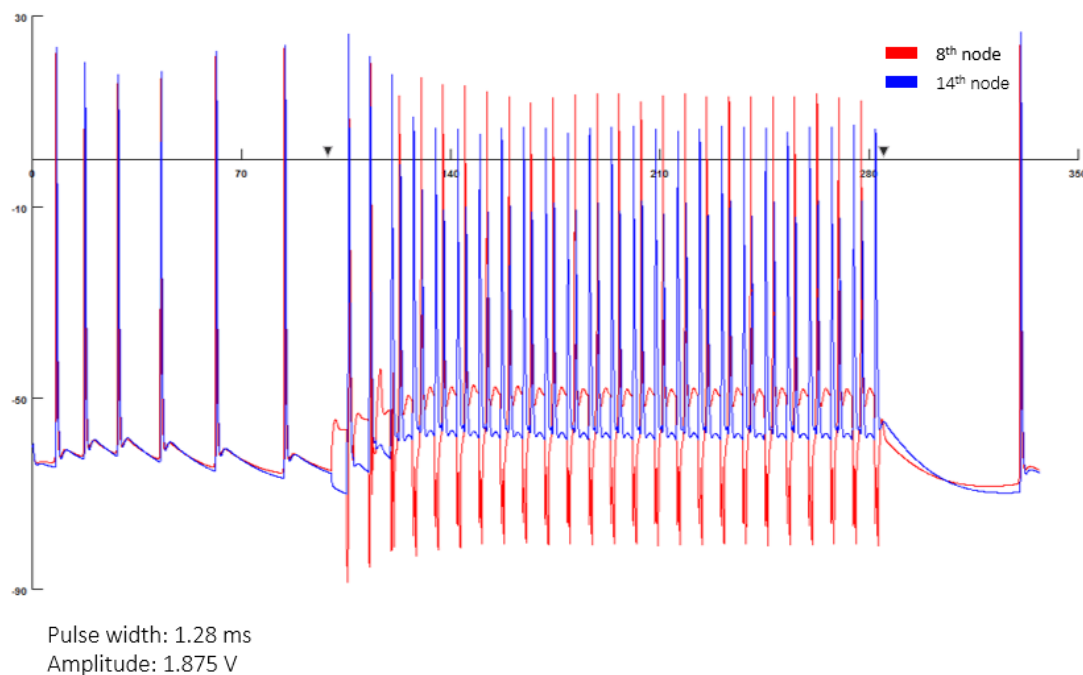


Figure 15 | Suprathreshold stimulation with the prepulse anode waveform. 25 pulses are delivered at 1.875 V (threshold is 1.171875 V), but the neuron fired 47 APs. Start and end of stimulation are marked with arrowheads on the time axis.

Biphasic waveforms show superiority of cathodic stimulation

Biphasic waveforms do not have a typical recharge phase. They are each composed of two stimulating pulses of opposite voltage: in biphasic cathode, the first stimulating pulse is cathodic and the second is anodic; in biphasic anode, the first stimulating pulse is anodic and the second is cathodic. Although they do not carry the typical long recharge phase of low amplitude, the two pulses charge balance each other. In this case, the second pulse is also an active recharge, as opposite to the passive recharge found in typical waveforms. Biphasic waveforms have previously been tested in a small clinical trial³⁷. Interestingly, results were rather contradictory: among the 8 patients tested, the biphasic waveform caused intolerable side effects in two, but provided significantly greater benefits than optimal clinical settings (in terms of UPDRS scores) for the six others³⁷.

Strength-duration curves for biphasic cathode and anode are practically superimposing each other (**Figure 16A**). The only difference is at the shortest pulse widths (under 0.06 ms) where, as usual, anodic stimulation is unable to activate the neuron (threshold > 10 V). When comparing with monophasic waveforms, we notice that the biphasic strength-duration curves are extremely alike the one for monophasic cathode (**Supplementary Figure 2**). They are only slightly deviating under 0.02 ms pulse width when the monophasic cathode strength-duration curve is a bit lower, i.e. weaker pulses are sufficient to activate the neuron. Consistently, chronaxies and rheobases are close between both versions of the biphasic waveforms, and similar to the monophasic cathode chronaxie and rheobase (cathodic rheobase: 0.542969 V; anodic rheobase: 0.480469 V; cathodic chronaxie: 0.26 ms; anodic chronaxie: 0.34 ms; rheobase and chronaxie for monophasic cathode: 0.542969 V and 0.22 ms). The most common initiation site for biphasic cathode is node 8 throughout the entire range of pulse widths (**Figure 16B**), which is what we observed with all cathodic waveforms up to now. Less usual, the most common initiation site during anodic stimulation is also node 8, and no switch is observed (**Figure 16C**).

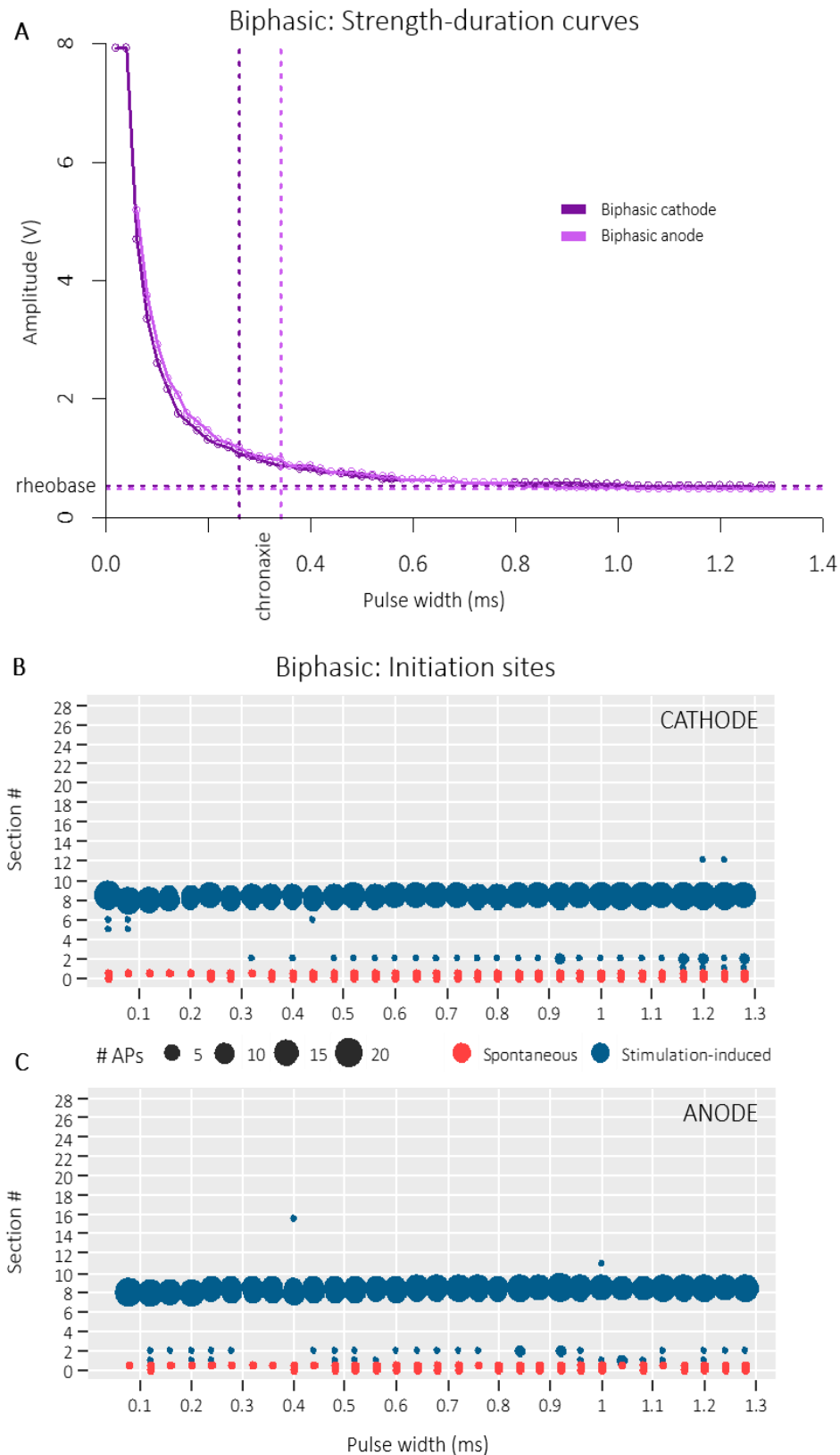


Figure 16 | Stimulation with the biphasic waveforms. **(A)** Strength-duration curves for biphasic cathode (dark red) and biphasic anode (light red). Biphasic cathode: rheobase = 0.542969 V, chronaxie = 0.26 ms. Biphasic anode: rheobase = 0.480469 V, chronaxie = 0.34 ms. **(B)** APs' initiation sites under biphasic cathode. **(C)** APs' initiation sites under biphasic anode. The area of each bubble is proportional to the number of APs fired at the section. Pink bubbles correspond to spontaneous APs, blue to stimulation-induced APs.

The biphasic setting distinctly shows in a single waveform the superior efficiency of cathodic stimulation. The model is seeking the weakest amplitude possible to evoke APs. In this situation, both phases have the same amplitude, it will thus choose, in a sense, to stimulate with the most efficient one. Cathodic stimulation being significantly more efficient than anodic, the cathodic pulse is preferred, whether it is the first phase or the second. Latency times confirm this (**Supplementary Figure 4**). For biphasic cathode, they follow the increase in pulse width. APs are thus fired toward the end of the first, cathodic phase. For biphasic anode, the slope of the latency time line is around 2: APs are fired toward the end of the second, also cathodic phase.

Even if the first anodic phase in anodic stimulation does not generate APs, it should hyperpolarise node 8, making it more reluctant to fire APs afterward. It is thus surprising that stronger amplitudes do not seem to be necessary to evoke APs in this setting. Slightly stronger amplitudes are necessary at short pulse widths, but this effect is not as large as expected, and dampens after 0.06 ms. Similarly to the postpulse anodic waveform, the answer may be the instantaneous switch between anodic and cathodic voltage. At the end of the anodic pulse, the activation gate is closed and the inactivation gate is partially or entirely open whether pulse width is short or long, respectively. When voltage switches to cathodic, the activation gate will be fast to open, and the inactivation gate slow to close. This may explain why amplitudes as low as those found for monophasic cathode (**Supplementary Figure 2**) are sufficient to activate node 8 in the biphasic anode setting. Additionally, this may also explain why slightly stronger amplitudes may be necessary when the pulse is very short (under 0.06 ms): the anodic pulse might be too short to entirely open the inactivation gate h , i.e. bring its value from 0.8 to 1. Thus, a slightly stronger second pulse may be necessary to evoke an AP.

Future directions

From what we have accomplished with this work, two broad future directions take shape and can be pushed forward in the future: further improving and testing the model in alternative stimulation settings, and moving towards clinical trial of these nonconventional parameters.

Towards further use of the model

Further development of the model

We have shown that this single-neuron model is sufficient to test some basic principles and formulate hypotheses. It is also useful to focus on more detailed effects such as the APs' initiation sites, which is rarely studied in literature. However, this model could be further developed to draw more conclusions on the effects of alternative DBS settings. A couple of suggestions can be made. For instance, we know that activation of the corticospinal tract within the internal capsule causes undesired muscle contractions (see *Deep brain stimulation* section). Therefore, an improvement of our model could be the addition of internal capsule fibres next to the STN projection neuron. As a first approximation, they can be modelled as a population of axons all duplicated from an initial template and transposed to form a tract³⁴. Alternatively, NEURON models of corticospinal neurons also exist in the ModelDB (for instance: Neymotin et al., 2017, accession number: 195615). Assuming correct transpositions of 3D coordinates and compatibility of parameters, it should be possible to partially or entirely merge one of these models to the current one.

Moreover, a population of STN projection neurons, potentially in addition with the corticospinal tract, could be simulated at once using NEURON²⁶. In a similar manner than for the corticospinal fibres, the current STN projection neuron can be used as template and be repeated and transposed within anatomical boundaries⁴⁰. Some populations are already implemented in this manner in the current model (see *The electric field files* section). Even though these different 3D locations are not meant to be tested simultaneously, their coordinates may be used to implement a multi-cell model. In this case, a condition for activation of the entire population should be added. For instance, a condition used in literature is the activation of 50% of the cells²⁵. By testing this condition on different versions of the population, i.e. alternative 3D coordinates within the same anatomical boundaries, a set of thresholds can be obtained. The mean at each pulse width can be used as data points for the strength-duration curves, with error bars corresponding to the standard error across populations²⁵. Improvements of that sort would make the model more realistic. However, they would greatly extend simulation time.

More research can also be performed to confirm some of the interpretations and preliminary results we presented. Namely, alternative 3D locations (see *The electric field files* section) and orientations could be tested to understand more precisely why node 8 and 14 fire predominantly. Fortunately, alternative neuron locations are already implemented in the current model and would be easy to test. Indeed, a loop in the main file can be used to switch neuron location at the end of each simulation. However, these neurons do not have different orientations, and creating alternative orientations would involve editing the sections coordinates. If the most common firing sites vary upon 3D location or orientation in the electric field, the reason is indeed the position relative to the electrode (**Supplementary Figure 1**). If they stay relatively constant, the main explanation must come from the neuron itself, for instance influence of the somatic firing. In this case, if some waveforms allow to pull the initiation site closer to the soma, it may have interesting benefits in terms of efficacy. Indeed, if a waveform specifically evokes APs close to the soma, it could avoid some of the unsought stimulation of fibres of passage responsible for most adverse effects (see *Aim of the study* section).

Moreover, our work tested a single morphology of the STN projection neuron. The thousands of neuron in the STN will have different morphologies which may change how they react to different stimulation waveforms. The current model encodes two alternative morphologies of the STN neuron which can easily be tested. The study from which these morphologies originated⁴⁶ reconstructed seventy-five single axon trajectories, classified into five broad types depending on their target. By following an analogue methodology to the current study, it should also be possible to add a few morphologies to the current model, at least representing each of the five types of STN neurons.

More practically, we have seen that the initial classification of the APs as spontaneous or stimulation-induced can be inadequate in certain situations (see *Prepulse waveforms* section). Even in more conventional settings, the initial model consistently misclassifies a very small number of spontaneous APs as stimulation-induced. Most previously published articles omit the soma and its spontaneous activity altogether^{34 36}. However, even if the soma by itself seems unaffected by stimulation, it may affect the behaviour of the axon, for instance by causing periodic hyperpolarisation when the somatic APs propagate (see *Monophasic waveforms* section). This particularity of the present model is thus valuable and should be conserved. Like we did for the initiation sites bubble graphs (see *Initiation sites bubble graph* section), a better classification of the APs would be based on the initiation site. Assuming thorough verification of the assumption that all somatic APs are spontaneous, this classification could be hardcoded directly in the main model file. It would ease its future use and allow even more precise estimation of the thresholds.

Further testing of nonconventional parameters

We have studied here the effects of some nonconventional waveforms on a STN projection neuron model. Thanks to our modifications, the model can easily be used to test other alternative waveforms and/or stimulation parameters. We can formulate some propositions based on literature.

A genetic algorithm was previously used to design the most energy-efficient waveform for stimulation of the mammalian myelinated axon³³. This waveform, resembling a truncated Gaussian curve, could be tested on the present STN projection neuron model. It would allow to check its efficiency in a situation closer to *in vivo* STN DBS than the original article³³. Nevertheless, a limitation of numerous studies, including the latter, is the assumption that energy efficiency is a good predictor of battery life. This might not be the case mainly because of the energy consumed by the electronic circuitry of the pulse generator³³. For instance, a saving of 50% energy use was shown to only extend battery life by 12% in one brand of pulse generators⁵⁴. Regardless, that would still add a valuable half a year to the typical lifetime of the device²⁶.

Promising results were also obtained with the addition of a gap, i.e. a brief time of null electrode voltage, between the stimulating pulse and the recharge phase²⁵. In this situation, safety aspects should carefully be taken into considerations and limit the range of gap durations which can be tested. Indeed, the goal of the balance of charge is the reversal of electrochemical reactions happening at the electrode/tissue interface. If the gap is too long, reactants diffuse away and cannot be recovered upon the recharge phase. This can be both damageable to the electrode and toxic to the surrounding cells. Gap duration is thus limited by the diffusion rate of the reactants²⁵. The authors of the latter study also see great potential in the combination of both waveforms, i.e. the addition of a gap to the genetic algorithm waveform³³. The effects of such type of waveforms on our model would be relatively easy to assess. In this setting, successive simulations could be performed at increasing gap duration instead of increasing pulse width. It would also be interesting to visualise how threshold varies as a function of gap length. Simple insertion of a gap between the two pulse phases also has the advantage of being readily implementable in existing DBS pulse generators, contrarily to the Gaussian waveform created by the genetic algorithm.

Similarly, we could also study the effects of varying ratios between the stimulating pulse and the recharge phase in the pre- and postpulse waveforms. In our work, both phases always had a fixed one-to-four ratio, i.e. the recharge phase was four times longer and four times weaker than the stimulating pulse. Thanks to our modifications, this model could easily be used to run series of successive simulations at increasing ratio. We could, for instance, run simulations from a five-to-one ratio, i.e. a prepulse waveform where the first recharge phase is five times longer and five times weaker than the stimulating pulse, up to five-to-one ratio, i.e. the postpulse equivalent, passing by one-to-one, which corresponds to the biphasic waveform.

A particularly interesting area of research that we could also explore with this model are the firing frequencies. Briefly, there is growing evidence showing that PD is associated with pathological synchronised oscillations in the beta range (11–30 Hz) in the STN⁵⁵. Coincidentally, levodopa seems to suppress STN's activity in the beta range⁵⁶, and clinical trials in which DBS was turned on only during period of elevated beta activity delivered major clinical benefits exceeding those obtained with standard continuous stimulation⁵⁷. Nevertheless, some contradictory results exist⁵⁸. They show the need for a more basic understanding of how the firing frequency of the STN neuron is affected by DBS. This model may be adequate for this application, allowing for precise investigation of the results obtained in patients. Although improvements would be necessary, some aspects of the pre- and post-stimulation frequencies calculations are already implemented. It would also be crucial to analyse if the pathological activity is satisfactorily modelled as it is now. Spontaneous activity of the model correctly replicates measurements made in the Parkinsonian macaque's STN (see *Morphology files* section). This is thus a first hint that it may well be the case.

Towards clinical use

This work is preceding the testing of nonconventional waveforms and/or parameters in patients implanted with DBS. Although clinical trials of nonconventional settings are relatively scarce, they are sufficient to prove feasibility in PD patients and give some insight about study design. Around 11 DBS settings can be tested with the patient during a single three-hour visit. The patient is blinded to the simulation settings, which are tested in a randomized order. Clinically-optimal settings are used as positive control and stimulation turned off as negative. Motor assessment are videotaped and rated by three persons: two raters, one blinded and one unblinded, present during testing, and one blinded rater via video recordings. Ratings of PD motor symptoms are performed with UPDRS part III. An accelerometer can also be used for scoring distinct types of tremors. Finally, gait can be more objectively assessed with walkway systems like GaitRide³⁷. Such clinical trials are planned in Prof Mc Laughlin's laboratory in the coming year.

With regard to the settings themselves, the biphasic cathodic waveform was previously tested and is considered safe³⁷. We can probably assume that the postpulse anodic waveform, due to its resemblance to the standard clinical waveform, is also safe to test. Waveforms not providing a balance of charge, i.e. monophasic, are not safe and cannot be tested (see *Stimulation parameters* section). As for the others, and especially when the pulse order is reversed, decision cannot only be based on computational modelling, and further experimental investigation may probably be necessary before considering pre-clinical application²⁵.

Conclusion

To briefly summarise our main achievements, we first brought several improvements to an existing model of the STN projection neuron under DBS. These allowed us to conveniently test a set of ten waveforms at a wide range of pulse widths, among which eight can be considered nonconventional. The main results we produced were the thresholds for activation, which were plotted as a function of pulse width in the form of strength-duration curves, and the precise APs' firing sites. Some waveforms displayed interesting behaviours that certainly deserve further investigation. Namely, the postpulse anodic waveform switched the most common firing site at short pulse widths to a node closer to the soma, without affecting the strength-duration curve. Moreover, preliminary results showed that the prepulse anodic waveform could be employed slightly suprathreshold to evoke two APs per pulse instead of one. Other findings included that the recharge phase of the clinical anodic waveform was not passive at long pulse widths, and that stimulation was always cathodic with the biphasic waveforms, no matter whether the first phase was anodic or cathodic.

This work is preceding the testing of nonconventional waveforms and/or parameters in PD patients implanted with DBS. It provides a computational model of the STN projection neuron which can readily be used to test countless combinations of nonconventional settings such as waveform, pulse width, frequency or gap length. By proposing possible mechanisms and examples on how to reason on the effects of waveform on stimulation, it also gives clues for the future interpretation of results in patients.

Finally, DBS is both a widely used therapy and a dynamic research field at the interface of neuroscience and engineering. The most exciting discoveries around this technology are probably to come. For instance, DBS is currently under clinical investigation for Alzheimer's disease^{59 60}. Our understanding of DBS mechanisms will also evolve with advances in fundamental brain research. The most recent of these is certainly the discovery that dendrites of cortical neurons fire APs at a rate up to ten-fold the somatic rate. This has far-reaching implications for neural coding that may change our understanding of the basal ganglia and thus of DBS mechanisms. The technology will also benefit from engineering research, such as the recent design of a supercapacitor for implantable devices which powers itself from heat, motion, and electrolytes in biological fluids. One day, it may well provide endless energy to implanted DBS pulse generators that would never need to be replaced.

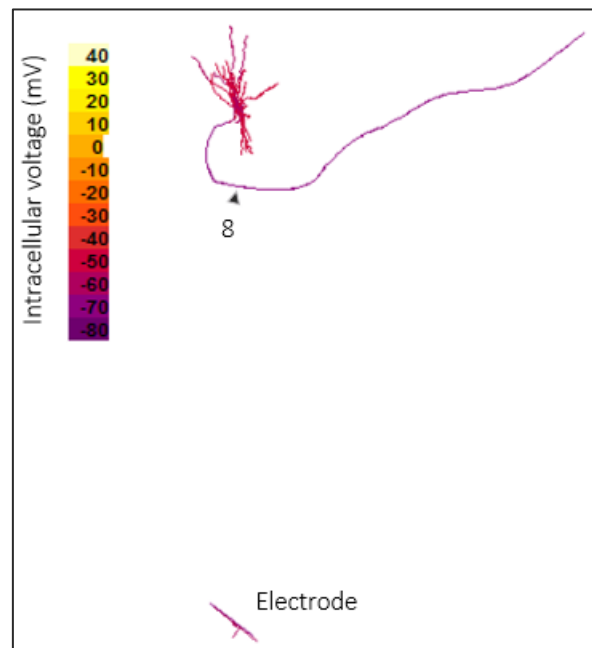
Bibliography

1. Kalia, L. V. & Lang, A. E. Parkinson's disease. *Lancet* **386**, 896–912 (2015).
2. de Lau, L. M. L. & Breteler, M. M. B. Epidemiology of Parkinson's disease. *Lancet Neurol.* **5**, 525–535 (2006).
3. Dorsey, E. R. *et al.* Projected Number of People With Parkinson Disease in the Most Populous Nations, 2005 Through 2030. *Neurology* **68**, 384–386 (2007).
4. Jankovic, J. Parkinson's disease: clinical features and diagnosis. *J. Neurol. Neurosurg. Psychiatry* **79**, 368–376 (2007).
5. Pezzoli, G. & Zini, M. Levodopa in Parkinson's disease: from the past to the future. *Expert Opin. Pharmacother.* **11**, 627–635 (2010).
6. Hickey, P. & Stacy, M. Deep brain stimulation: A paradigm shifting approach to treat Parkinson's disease. *Front. Neurosci.* **10**, 1–11 (2016).
7. Rea, P. in *Essential Clinical Anatomy of the Nervous System* 161–176 (Elsevier, 2015). doi:10.1016/B978-0-12-802030-2.00002-9
8. Xie, C.-L. *et al.* Effects of neurostimulation for advanced Parkinson's disease patients on motor symptoms: A multiple-treatments meta-analysis of randomized controlled trials. *Sci. Rep.* **6**, 1–11 (2016).
9. Williams, N. R., Foote, K. D. & Okun, M. S. Subthalamic Nucleus Versus Globus Pallidus Internus Deep Brain Stimulation: Translating the Rematch Into Clinical Practice. *Mov. Disord. Clin. Pract.* 24–35 (2014). doi:10.1002/mdc3.12004
10. Miocinovic, S., Somayajula, S., Chitnis, S. & Vitek, J. L. History, applications, and mechanisms of deep brain stimulation. *JAMA Neurol.* **70**, 163–71 (2013).
11. Fahn, S. & Elton, R. in *Recent Developments in Parkinson's Disease* **2**, 153–163, 293–304 (Macmillan Health Care Information, 1987).
12. Deuschl, G. *et al.* A Randomized Trial of Deep-Brain Stimulation for Parkinson's Disease. *N. Engl. J. Med.* **355**, 896–908 (2006).
13. Hacker, M. L. *et al.* Subthalamic Nucleus Deep Brain Stimulation May Reduce Medication Costs in Early Stage Parkinson's Disease. *J. Parkinsons. Dis.* **6**, 125–131 (2016).
14. Becerra, J. E. *et al.* Economic Analysis of Deep Brain Stimulation in Parkinson's Disease: Systematic Review of the Literature. *Value Heal.* **19**, A302–A303 (2016).
15. Fakhar, K. *et al.* Management of Deep Brain Stimulator Battery Failure: Battery Estimators, Charge Density, and Importance of Clinical Symptoms. *PLoS One* **8**, 1–8 (2013).
16. Troche, M. S. *et al.* Swallowing outcomes following unilateral STN vs. GPi surgery: A retrospective analysis. *Dysphagia* **29**, 425–431 (2014).
17. Cyron, D. Mental Side Effects of Deep Brain Stimulation (DBS) for Movement Disorders: The Futility of Denial. *Front. Integr. Neurosci.* **10**, 1–4 (2016).
18. Johnson, M. D., Miocinovic, S., McIntyre, C. C. & Vitek, J. L. Mechanisms and Targets of Deep Brain Stimulation in Movement Disorders. *Neurotherapeutics* **5**, 294–308 (2008).
19. McIntyre, C. C. & Foutz, T. J. in *Handbook of Clinical Neurology* **116**, 55–61 (Elsevier, 2013).
20. Groiss, S. J., Wojtecki, L., Südmeyer, M. & Schnitzler, A. Deep brain stimulation in Parkinson's disease. *Ther. Adv. Neurol. Disord.* **2**, 379–391 (2009).
21. McIntyre, C. C., Grill, W. M., Sherman, D. L. & Thakor, N. V. Cellular Effects of Deep Brain Stimulation : Model-Based Analysis of Activation and Inhibition Cellular Effects of Deep Brain Stimulation : Model-Based Analysis of Activation and Inhibition. *J. Neurophysiol.* **91**, 1457–1469 (2004).
22. Perlmuter, J. S. & Mink, J. W. Deep Brain Stimulation. *Annu. Rev. Neurosci.* **29**, 229–257 (2006).
23. Kringelbach, M. L., Jenkinson, N., Owen, S. L. F. & Aziz, T. Z. Translational principles of deep brain stimulation. *Nat. Rev. Neurosci.* 623–635 (2007). doi:10.1038/nrn2196
24. Grill, W. & Mortimer, T. Stimulus waveforms for selective neural

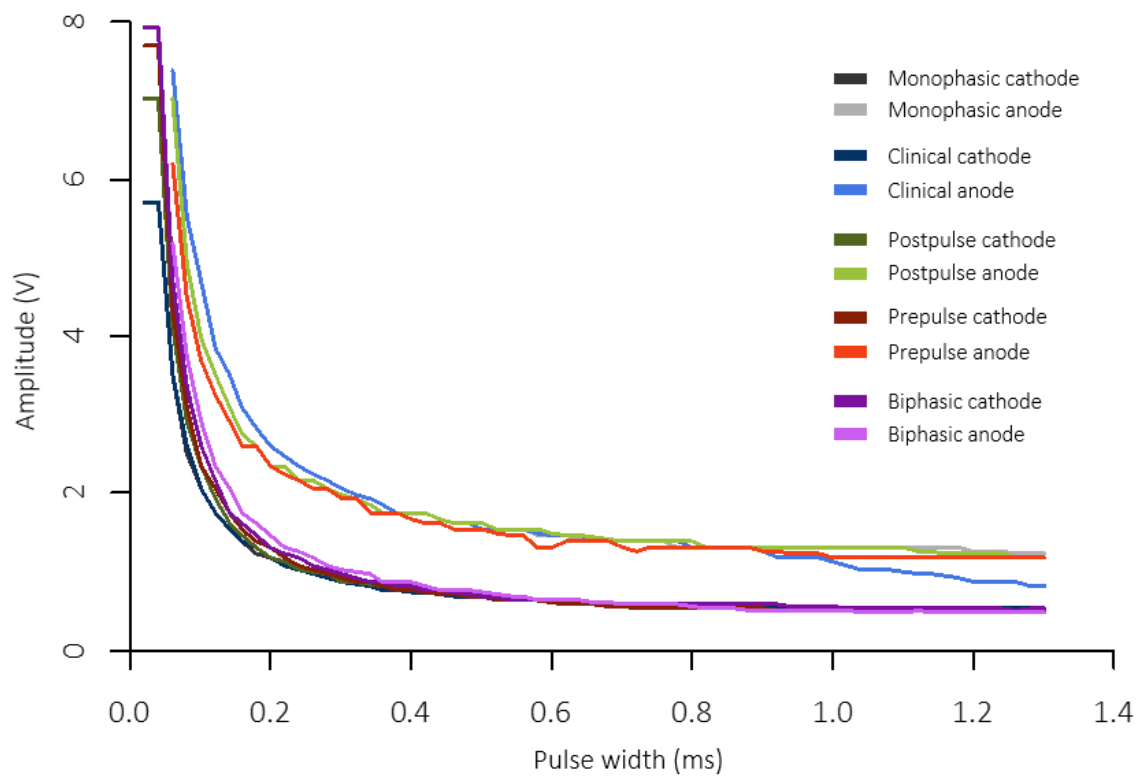
- stimulation. *IEEE Eng. Med. Biol. Mag.* 375–385 (1995).
25. Hofmann, L., Ebert, M., Tass, P. A. & Hauptmann, C. Modified pulse shapes for effective neural stimulation. *Front. Neuroeng.* **4**, 1–10 (2011).
26. Foutz, T. J. & McIntyre, C. C. Evaluation of novel stimulus waveforms for deep brain stimulation. *J. Neural Eng.* **7**, 1–10 (2010).
27. Hines, M. L. & Carnevale, N. T. The NEURON simulation environment. *Neural Comput.* **9**, 1179–1209 (1997).
28. Rall, W. & Agmon-Snir, H. in *Methods in Neuronal Modeling: From Ions to Networks* 27 (MIT Press, 1998).
29. Hodgkin, A. L. & Huxley, A. F. A Quantitative Description of Membrane Current and Its Application to Conduction and Excitation in Nerves. *J. Physiol.* **117**, 500–544 (1952).
30. Carnevale, N. T. & Hines, M. L. *The NEURON Book*. (Cambridge University Press, 2006).
31. UCLA Health. Deep Brain Stimulation. (2017). Available at: <http://neurosurgery.ucla.edu/dbs/deep-brain-stimulation>. (Accessed: 9th May 2017)
32. Pouratian, N., Thakkar, S., Won, K. & Bronstein, J. M. Deep brain stimulation for the treatment of Parkinson's disease: efficacy and safety. *Degener. Neurol. Neuromuscul. Dis.* **2**, 1–16 (2012).
33. Wongsarnpigoon, A. & Grill, W. M. Energy-efficient waveform shapes for neural stimulation revealed with a genetic algorithm. *J. Neural Eng.* **7**, 1–11 (2010).
34. Reich, M. M. *et al.* Short pulse width widens the therapeutic window of subthalamic neurostimulation. *Ann. Clinical Transl. Neurol.* **2**, 427–432 (2015).
35. Bocker, D. T. *et al.* Improved efficacy of temporally non-regular deep brain stimulation in Parkinson's disease. *Exp. Neurol.* **239**, 60–67 (2013).
36. Sahin, M. & Tie, Y. Non-rectangular waveforms for neural stimulation with practical electrodes. *J. Neural Eng.* **4**, 227–233 (2007).
37. Akbar, U. *et al.* Randomized, Blinded Pilot Testing of Nonconventional Stimulation Patterns and Shapes in Parkinson's Disease and Essential Tremor: Evidence for Further Evaluating Narrow and Biphasic Pulses. *Neuromodulation* **19**, 343–356 (2016).
38. Krouchev, N. I., Danner, S. M., Vinet, A., Rattay, F. & Sawan, M. Energy-optimal electrical-stimulation pulses shaped by the least-action principle. *PLoS One* **9**, 1–24 (2014).
39. McDougal, R. A. *et al.* Twenty years of ModelDB and beyond: building essential modeling tools for the future of neuroscience. *J. Comput. Neurosci.* 1–10 (2016). doi:10.1007/s10827-016-0623-7
40. Miocinovic, S. *et al.* Computational analysis of subthalamic nucleus and lenticular fasciculus activation during therapeutic deep brain stimulation. *J. Neurophysiol.* **96**, 1569–1580 (2006).
41. Johnson, C., Holmes, W. R., Brown, A. & Jung, P. Minimizing the caliber of myelinated axons by means of nodal constrictions. *J. Neurophysiol.* **114**, 1874–1884 (2015).
42. Johnston, D., Gray, R. & Miao-Sin Wu, S. *Foundations of Cellular Neurophysiology*. (MIT Press, 1999).
43. Bevan, M. D. & Wilson, C. J. Mechanisms underlying spontaneous oscillation and rhythmic firing in rat subthalamic neurons. *J. Neurosci.* **19**, 7617–7628 (1999).
44. Gillies, A. & Willshaw, D. Membrane Channel Interactions Underlying Rat Subthalamic Projection Neuron Rhythmic and Bursting Activity. *J. Neurophysiol.* **95**, 2352–2365 (2006).
45. Wichmann, T., Kliem, M. A. & Soares, J. Slow oscillatory discharge in the primate basal ganglia. *J. Neurophysiol.* **87**, 1145–1148 (2002).
46. Sato, F., Parent, M., Levesque, M. & Parent, A. Axonal branching pattern of neurons of the subthalamic nucleus in primates. *J. Comp. Neurol.* **424**, 142–152 (2000).
47. Wickham, H. Reshaping Data with the {reshape} Package. *J. Stat. Softw.* **21**, 1–20 (2007).
48. Wickham, H. & Francois, R. dplyr: A Grammar of Data Manipulation. (2016).
49. RStudio Team. RStudio: Integrated Development Environment for R. (2015).
50. Wickham, H. *ggplot2: Elegant Graphics for Data Analysis*. (2009).
51. Malmivuo, J. & Plonsey, R. in *Bioelectromagnetism: Principles and Applications of Bioelectric and Biomagnetic Fields* (Oxford Scholarship

- Online, 1995). doi:DOI:10.1093/acprof:oso/9780195058239.003.0021
52. Burke, B. Y. W. & Ginsborg, B. L. The electrical properties of the slow muscle fibre membrane. *J. Physiol.* **132**, 586–598 (1956).
53. Neymotin, S. A. *et al.* Optimizing computer models of corticospinal neurons to replicate in vitro dynamics. *J. Neurophysiol.* **117**, 148–162 (2017).
54. Anheim, M. *et al.* Lifetime of Itrel II pulse generators for subthalamic nucleus stimulation in Parkinson's disease. *Mov. Disord.* **22**, 2436–2439 (2007).
55. Weinberger, M., Hutchison, W. D. & Dostrovsky, J. O. Pathological subthalamic nucleus oscillations in PD: Can they be the cause of bradykinesia and akinesia? *Exp. Neurol.* **219**, 58–61 (2009).
56. Priori, A. *et al.* Rhythm-specific pharmacological modulation of subthalamic activity in Parkinson's disease. *Exp. Neurol.* **189**, 369–379 (2004).
57. Little, S. & Brown, P. The functional role of beta oscillations in Parkinson's disease. *Park. Relat. Disord.* **20S1**, S44–S48 (2014).
58. Foffani, G. *et al.* Subthalamic oscillatory activities at beta or higher frequency do not change after high-frequency DBS in Parkinson's disease. *Brain Res. Bull.* **69**, 123–130 (2006).
59. NIH - National Institute on Aging. ADvance Deep Brain Stimulation in Patients with Mild Probable Alzheimer's Disease. *ClinicalTrials.gov* (2012). Available at: <https://www.nia.nih.gov/alzheimers/clinical-trials/advance-deep-brain-stimulation-patients-mild-probable-alzheimers-disease>.
60. Lozano, A. M. *et al.* A Phase II Study of Fornix Deep Brain Stimulation in Mild Alzheimer's Disease. *J. Alzheimer's Dis.* **54**, 777–787 (2016).
61. Fix, J. D. in *Neuroanatomy (Board Review Series)* 274–281 (Wulter's Kluwer & Lippincott Williams & Wilkins, 2008).
62. UC Regents. UC Davis tests deep brain stimulation as a treatment for cognitive changes in Parkinson's. (2015).
63. Häggström, M. Basal ganglia circuits.svg. *Wikipedia* (2010). Available at: https://en.wikipedia.org/wiki/Basal_ganglia#/media/File:Basal_ganglia_circuits.svg. (Accessed: 8th May 2017)
64. Radević, S. File: Rheobase chronaxie.png. *Wikimedia Commons* (2012). Available at: https://commons.wikimedia.org/wiki/File:Rheobase_chronaxie.png. (Accessed: 18th May 2017)
65. Poliak, S. & Peles, E. The local differentiation of myelinated axons at nodes of Ranvier. *Nat. Rev. Neurosci.* **4**, 968–980 (2003).

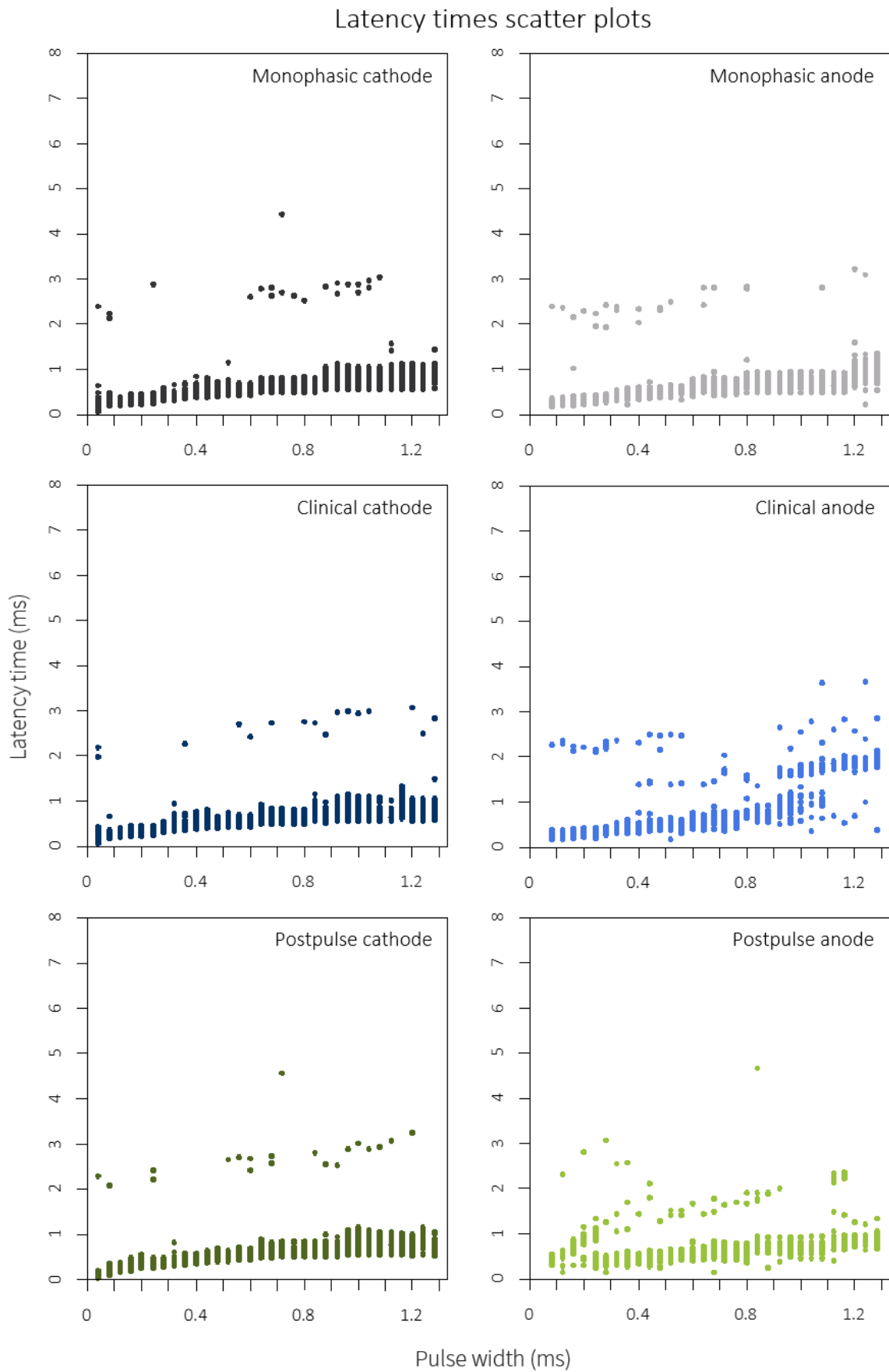
Supplementary figures



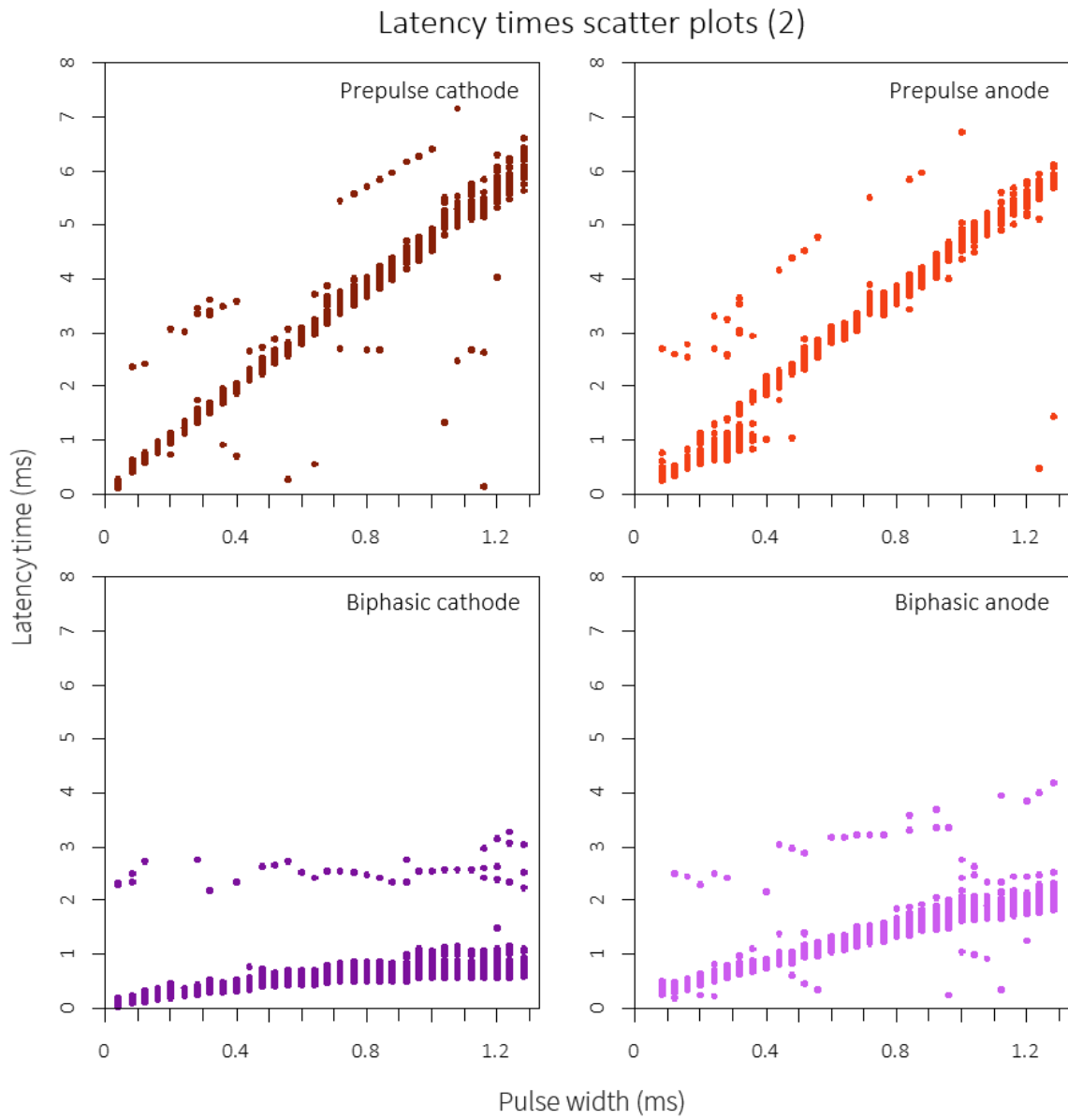
Supplementary Figure 1 | Position of the neuron, and specifically node 8, relative to the electrode.



Supplementary Figure 2 | The ten strength-duration curves superimposed. Monophasic cathode (dark grey) and anode (light grey) cannot be seen properly but follow closely the curves for clinical cathode (dark blue) and postpulse anode (light green), respectively.



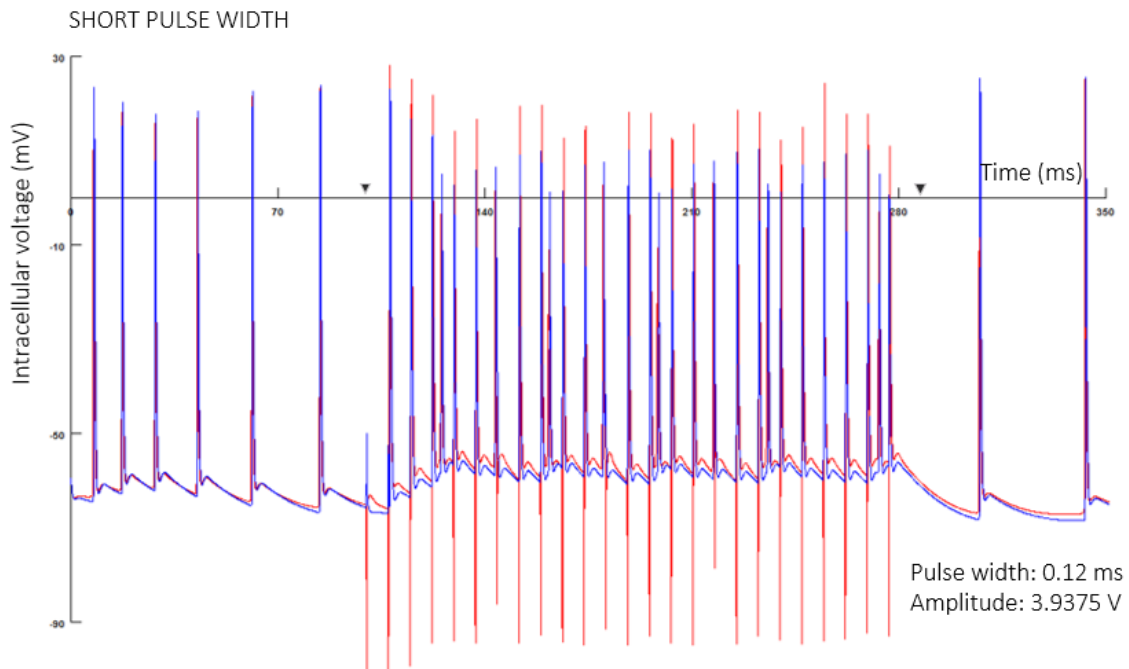
Supplementary Figure 3 | Latency times scatter plots for the monophasic, clinical and postpulse cathodic (right column) and anodic (left column) waveforms.



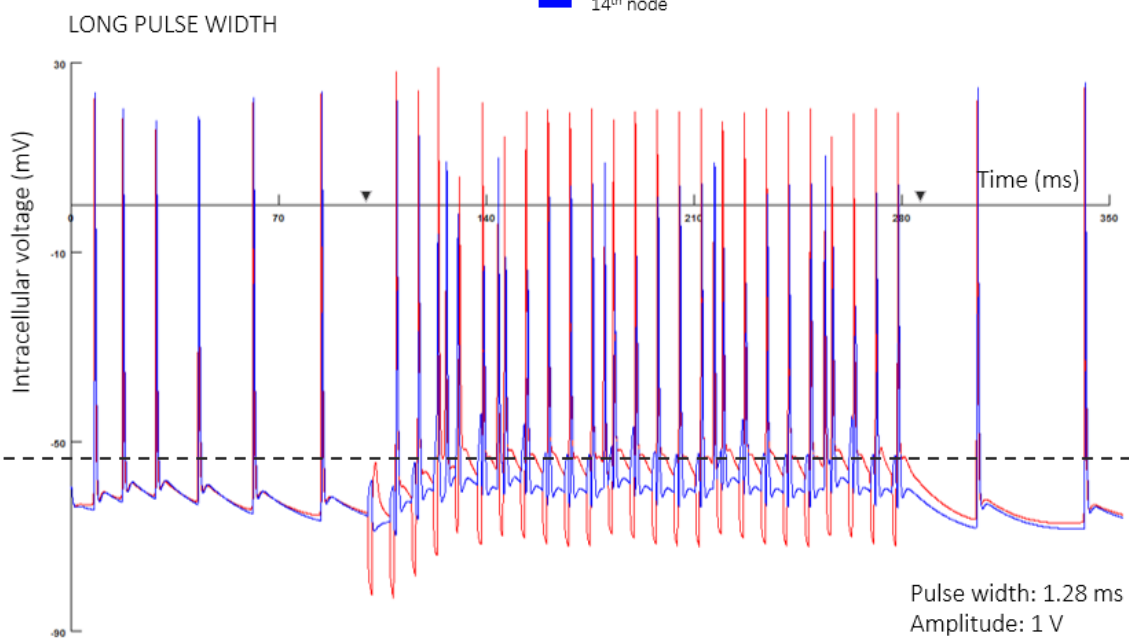
Supplementary Figure 4 | Latency times scatter plots for the prepulse and biphasic cathodic and anodic waveforms.

Clinical anode: node 8 & node 14 vs. time

A



B



Supplementary Figure 5 | Intracellular voltage at node 8 and node 14 as a function of time under clinical anodic stimulation, slightly suprathreshold. **(A)** At short pulse width: pulse width = 0.12 ms, amplitude = 3.9375 V (threshold amplitude = 3.843750 V). **(B)** At long pulse width: pulse width = 1.28 ms, amplitude = 1 V (threshold amplitude = 0.814453 V). The dashed black line indicates the maximum voltage at node 8 under short pulses (not taking into account APs). Notice how depolarisation at node 8 reaches higher levels under long pulse widths. Start and end of stimulation are marked by arrowheads on the time axes.

François Kroll
Master's Thesis

